RICE UNIVERSITY

Computational Study of Electronic and Transport Properties of Novel Boron and Carbon Nano-Structures

by

Arta Sadrzadeh

A THESIS SUBMITTED IN PARTIAL FULFILLMENT OF THE REQUIREMENTS FOR THE DEGREE

Doctor of Philosophy

APPROVED, THESIS COMMITTEE:

Boris I. Yakobson, Professor, Chair
Mechanical Engineering and Materials Science

Pulickel M. Ajayan, Professor
Mechanical Engineering and Materials Science

Junichiro Kono, Professor
Electrical and Computer Engineering

HOUSTON, TEXAS
DECEMBER 2012

ABSTRACT

Computational Study of Electronic and Transport Properties of Novel Boron and Carbon Nano-Structures

By

Arta Sadrzadeh

In the first part of this dissertation, we study mainly novel boron structures and their electronic and mechanical properties, using *ab initio* calculations. The electronic structure and construction of the boron buckyball B_{80}, and boron nanotubes as the α-sheet wrapped around a cylinder are studied. The α-sheet is considered so far to be the most stable structure energetically out of the two dimensional boron assemblies. We will argue however that there are other sheets close in energy, using cluster expansion method. The boron buckyball is shown to have different possible isomers. Characterization of these isomers according to their geometry and electronic structure is studied in detail. Since the B_{80} structure is made of interwoven double-ring clusters, we also investigate double-rings with various diameters. We investigate the properties of nanotubes obtained from α-sheet. Computations confirm their high stability and identify mechanical stiffness parameters. Careful relaxation reveals the curvature-induced buckling of certain atoms off the original plane. This distortion opens up the gap in narrow tubes, rendering them semi-conducting. Wider tubes with the diameter $d \gtrsim 1.7$ nm retain original metallic character of the α-sheet. We conclude this part by investigation into hydrogen storage capacity of boron-rich compounds, namely the metallacarboranes. In the second part of dissertation, we switch our focus to electronic

and transport properties of carbon nano-structures. We study the application of carbon nanotubes as electro-chemical gas sensors. The effect of physisorption of NO_2 gas molecules on electron transport properties of semi-conducting carbon nanotubes is studied using *ab initio* calculations and Green's function formalism. It is shown that upon exposure of nanotube to different concentrations of gas, the common feature is the shift in conductance towards lower energies. This suggests that physisorption of NO_2 will result in a decrease (increase) in conductance of p-type (n-type) nanotubes with Fermi energies close to the edge of valence and conduction band. Finally we study the effect of torsion on electronic properties of carbon nano-ribbons, using helical symmetry of the structures.

Acknowledgements

My sincere appreciation goes to my advisor, Dr. Boris I. Yakobson. Throuout my studies here at Rice, Dr. Yakobson provided invaluable guidance on my research. I am certain that his effect as a mentor as well, will help me in my future career.

Great thanks to the thesis committee members, Dr. Pulickel M. Ajayan and Dr. Junichiro Kono, for their time. I am also thankful to my colleagues for discussions and collaborations. They are in alphabetical order: Morteza Bankehsaz, Ksenia Bets, Somnath Bhowmick, Alex Dobrinsky, Amir A. Farajian, Ming Hua, Kun Jiao, Yu Lin, Yuanyue Liu, Evgeni S. Penev, Olga V. Pupysheva, Abhishek K. Singh, Nevill G. Szwacki, Fangbo Xu, and Zhiping Xu. With all due respect, I omit the titles, and I am sorry if I forgot to mention someone. Last, but not least, I am deeply grateful to my family and my wife, Tiffany, for their support and encouragement.

Contents

List of Figures

List of Tables

Chapter 1
Introduction

1.1 Boron

Atomic boron is the only element except carbon that can build molecules of any size by covalently bonding to itself [1]. Due to sp^2 hybridization of the valence electrons in most boron compounds and large coordination number, boron prefers to form strong directional bonds with various elements. Boron makes multi-center bonds, where a pair of electrons is shared between more than two atoms. This is due to the fact that there are more valence orbitals (s, p_x, p_y, p_z) available than there are electrons ($2s^2 2p^1$), which makes boron electron deficient. In other words, the bonding molecular orbitals are not fully occupied. These characteristics lead to a large diversity in boron nanostructures: clusters, nanowires and nanotubes [2-5].

There are four phases for the bulk boron; α- and β-rhombohedral [6, 7], α-tetragonal [8] and γ-orthorhombic [9]. α-rhombohedral is made of B_{12} units, with lattice constant 5.30 Å, and angle 58.13° [10] (Fig. 1.1). Each B_{12} icosahedron is slightly distorted due to Jahn-Teller effect, reducing the symmetry from I_h to D_{3d} [10]. β-rhombohedral has a somewhat complicated unit cell, composed of 105 atoms, with lattice constant 10.15 Å, and angle 65.17° [7, 11]. A striking B_{84} structure with icosahedral symmetry can be identified in β-rhombohedral [12]. α-tetragonal unit cell is made of 50 atoms, with lattice constants; a = 8.75 Å, and c = 5.06 Å [10]. It contains four B_{12} icosahedra and two isolated 4-bonded atoms. Finally, γ-orthorhombic has a unit cell of 28 atoms with a = 5.05 Å, b = 5.62 Å and c = 6.99 Å. It is stable under high pressure (19-89 GPa). Its structure resembles NaCl-type structure, with slightly distorted B_{12} icosahedra (2) and

B_2 pairs (2) playing the role of anions and cations, respectively. Recently by means of *ab initio* studies, it has been shown that α-rhombohedral is more stable than β-rhombohedral at zero temperature [13]. α-rhombohedral bulk is a semi-conducting material with energy gap of ~2 eV [10].

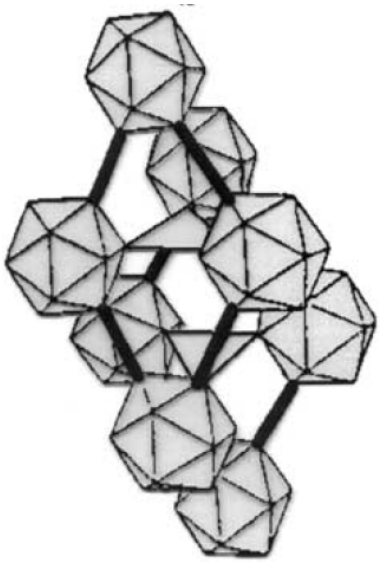

Figure 1.1 The lattice structure of α-rhombohedral bulk boron. Each atom is covalently bonded to 5 intra-icosahedral, and 1 or 2 inter-icosahedral atoms (from [2]).

Systematic experimental and theoretical work on non-crystalline boron started in eighties. Mass spectra of boron clusters were obtained in a series of experimental studies performed by Hanley et al. [14, 15]. Further important experimental study on the mass spectra was performed by La Placa et al. [16]. The method used was laser ablation of hexagonal boron nitride, and the mass of the clusters was separated by a time-of-flight technique. The experimental data showed “magic numbers” by boron cations of the size of 5, 7, 10 and 11.

Based on series of *ab-intio* simulations, Boustani proposed an "Aufbau Principle", stating that the most stable boron clusters can be constructed using two basic units: pentagonal and hexagonal pyramids, B_6 and B_7, respectively [17].

The boron clusters up to the size of 20 atoms have been shown to fall into two major categories: quasi-planar and compact. Fig. 1.2 shows different isomers with 14 or fewer atoms [2].

Kiran et al. showed that planar to tubular structure transition occurs at B_{20} [4]. Further theoretical studies lead by Boustani showed that indeed tubular structures (more precisely, double ring structures) are energetically favorable for larger clusters [18-20].

Aromaticity of small boron clusters has been studied by Zhai et al. [21]. It is shown that aromatic (planar) boron clusters possess more circular shapes whereas anti-aromatic ones are elongated.

Such structures should have a wide variety of applications [1]. One possible application is in cancer therapy. Boron in nature consists of the isotopes ^{10}B (19.6%) and ^{11}B (80.4%). The ^{10}B isotope has a special property that has long been exploited in nuclear reactors, namely, it has very high neutron absorption cross section (3835 barns) [22]. The reaction of ^{10}B with thermal neutron generates ^{7}Li and α particles, with latter having energies that make them lethal to nearby cell [22]. This aspect alone makes search for boron clusters of different shape, size, and cell-penetration ability very important. Another important and recently discussed possibility is in use of boron (with proper addition of metal atoms) clusters for efficient hydrogen storage [23].

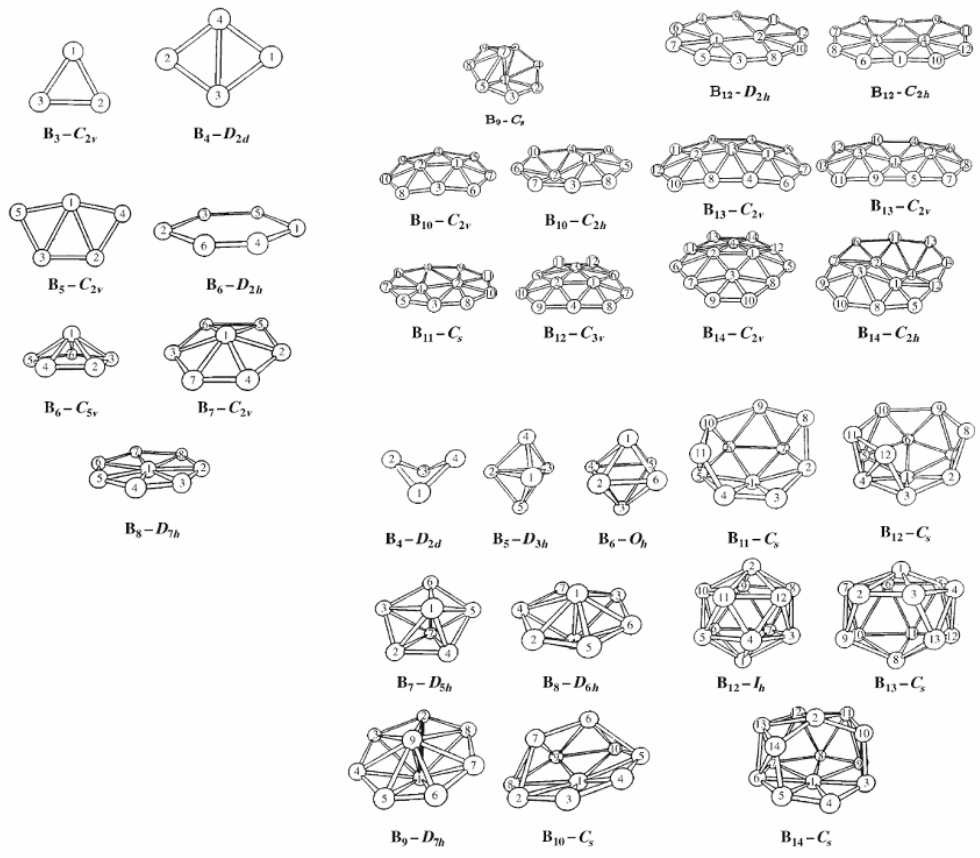

Figure 1.2 Structure and symmetry of boron clusters with 14 atoms or fewer (from [2]).

Rotary motion along a molecular axis, controllable by a single electron transfer or photoexcitation, has been proposed for metallacarboranes (Fig. 1.3) [24]. Existence of this or possibly other boron derived molecular motors has been sought for many years, as a parallel to biological motors that can be powered by light or electrical energy, rather than ATP.

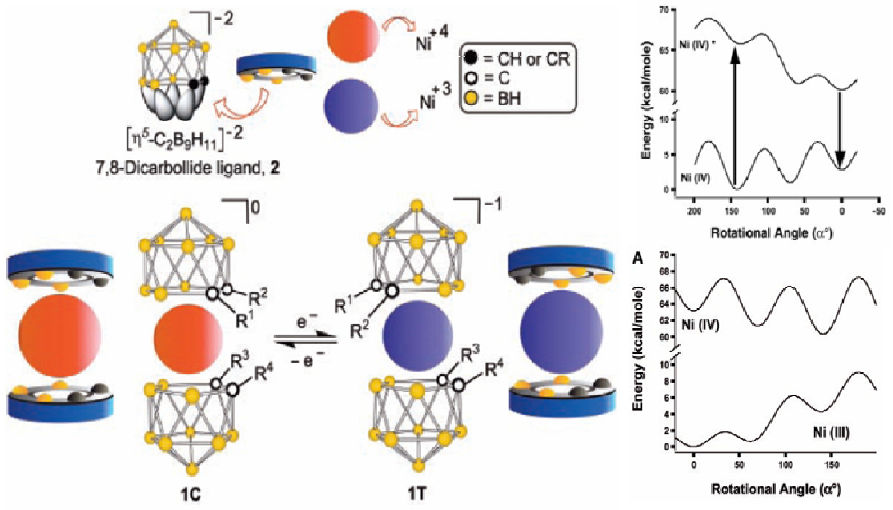

Figure 1.3 (Left) Illustration of rotor configurations of Ni(IV) (1C) and Ni(III) (1T) and the structural modules from which they are constructed. Structure 1T is defined with rotation angle 0°. R^1, R^2, R^3 and R^4 represent H here. (Right) Calculated energy of the ground and excited electronic state of the neutral Ni(IV) configuration as a function of rotation angle (figure reassembled from Ref. [24]).

1.2 History of Carbon Nanotubes

Carbon nanotubes were first discovered in 1991 by Iijima from NEC laboratories in Japan [25]. The first nanotubes discovered were made of several concentric cylindrical-

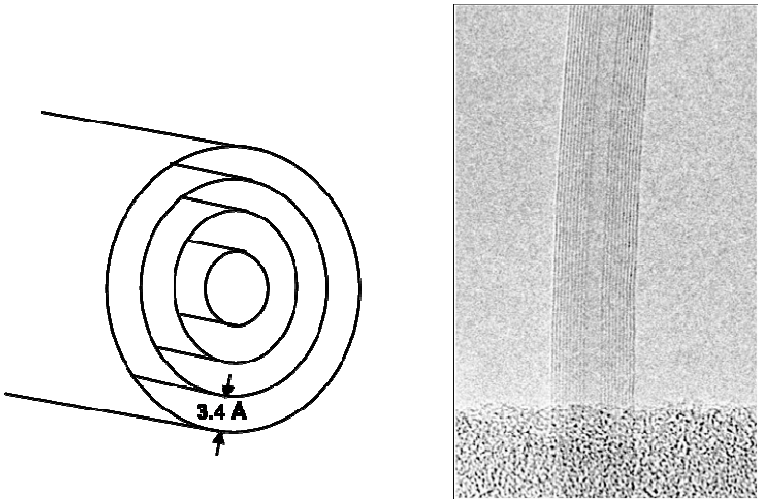

Figure 1.4 Schematic (left) and high resolution TEM image (right, from [26])of Multiwall carbon nanotubes.

like shells, separated by about 3.4 Å as in conventional graphite materials (Fig. 1.4). These multiwall nanotubes (MWNTs) were synthesized with diameters ranging from a few nanometers to several hundred nanometers for the inner and outer shells, respectively. As for the length, MWNTs extending over several microns are currently synthesized.

Shortly after the discovery of multiwall carbon nanotubes, single-wall carbon nanotubes (SWNTs) were synthesized using arc-discharge methods with transition-metal catalysts [27, 28]. A carbon nanotube made of a single graphite layer (the graphene sheet) rolled up into a hollow cylinder is called a single-wall nanotube. These tubes have quite small and uniform diameter, on the order of 1 nm. This unprecedentedly small diameter, combined with the crystalline perfection of the atomic network, explains why these objects were quickly considered as the ultimate carbon-based 1D systems. Crystalline ropes (or bundles) of SWNTs, with each rope containing tens to hundreds of tubes of similar diameter, closely packed in a hexagonal configuration, have also been synthesized using a laser vaporization method [29] and arc-discharge and chemical vapor deposition (CVD) techniques.

1.3 Structure of Carbon Nanotubes

In this section we introduce the basic concepts and parameters that determine the properties of carbon nanotubes. Fig. 1.5 illustrates the cutting of graphene to form a (5,3) nanotube. The so-called chiral vector $\boldsymbol{C_h}$ goes around the circumference of the rolled up tube. There are two parameters that control the microscopic structure of a nanotube, its diameter and its chiral angle or twist along the axis. Both are specified completely by $\boldsymbol{C_h}$, which is normally given in terms of the graphene lattice vectors $\boldsymbol{a}_1$ and $\boldsymbol{a}_2$; $\boldsymbol{C_h} = n_1\boldsymbol{a}_1 +$

$n_2\boldsymbol{a}_2$, where (n_1, n_2) are called the chiral index of a tube or, briefly, the chirality. A tube is characterized by (n_1, n_2). The diameter of a tube is given by

$$d_t = \frac{a}{\pi}\sqrt{n_1^{\,2} + n_2^{\,2} + n_1 n_2} \tag{1.3.1}$$

where a = 2.49 Å is the lattice constant of graphene sheet. The angle made between the chiral vector $\boldsymbol{C_h}$ and lattice vector $\boldsymbol{a}_1$, is given by:

$$Cos\theta = \frac{2n_1 + n_2}{2\sqrt{n_1^{\,2} + n_2^{\,2} + n_1 n_2}} \tag{1.3.2}$$

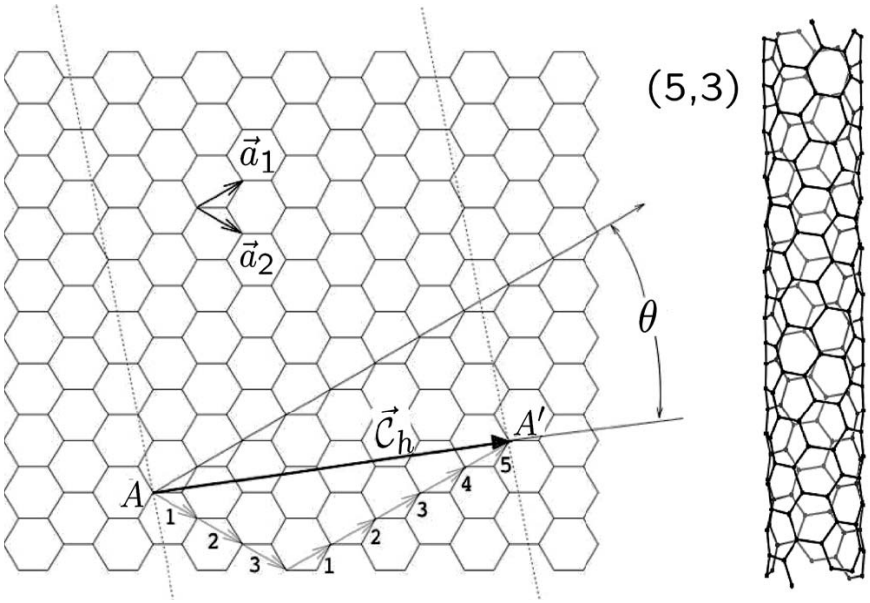

Figure 1.5 Graphene sheet honey-comb lattice with lattice vectors $\boldsymbol{a}_1$ and $\boldsymbol{a}_2$. Chiral vector $\boldsymbol{C_h}$ represents how the grapherne sheet is wrapped to form a nanotube ((5, 2) in this case). The angle θ which is made between $\boldsymbol{C_h}$ and $\boldsymbol{a}_1$ is called the chiral angle (from [30]).

The translational vector of the rolled up nanotube is given by: $\boldsymbol{T} = t_1\boldsymbol{a}_1 + t_2\boldsymbol{a}_2$, where

$$t_1 = \frac{n_1 + 2n_2}{d_R}, t_2 = -\frac{2n_1 + n_2}{d_R} \tag{1.3.3}$$

and d_R is the greatest common divisor of ($n_1 + 2n_2$) and ($2n_1 + n_2$). The number of carbon atoms per unit cell of the nanotube which is twice the number of hexagons N is given by:

$$N_C = 2N = \frac{4\left(n_1^2 + n_2^2 + n_1 n_2\right)}{d_R} \qquad (1.3.4)$$

The special case where $n_1 = n_2 = n$ is called armchair, and $n_2 = 0$ is called zigzag nanotube (Fig. 1.6). The chiral angle changes from $\theta = 0$ for zigzag to $\theta = 30°$ for armchair nanotubes.

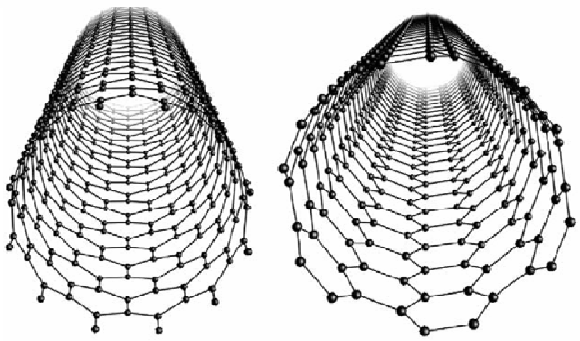

Figure 1.6 Atomic structure of (12,0) zigzag (left), and (6,6) armchair (right) nanotubes (from [30]).

1.4 Electronic Properties of Carbon Nanotubes

Carbon atoms in nanotubes form two types of bonds, σ and π, which in analogy with graphene, exhibit sp^2 hybridization. Assuming z direction is perpendicular to the surface of the nanotube, Atomic s, p_x and p_y orbitals combine to form bonding σ and antibonding σ^* states, and p_z orbitals form bonding π and antibonding π^* states. Since CNTs are rolled up graphene sheets, we start with the electronic structure of the graphene sheet. Fig. 1.7 illustrates its Brillouin Zone (BZ) and band structure.

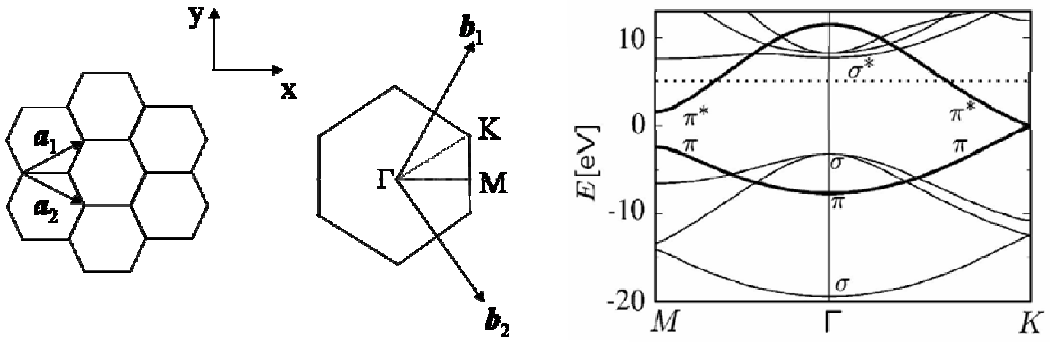

Figure 1.7 Brillouin zone (middle) and band structure (right) of graphene sheet. $b_1 = b\left(\frac{1}{2}, \frac{\sqrt{3}}{2}\right), b_2 = b\left(\frac{1}{2}, -\frac{\sqrt{3}}{2}\right), where; b = \frac{4\pi}{a\sqrt{3}}$ are the reciprocal lattice unit vectors. Dashed line in the band structure plot indicates the work function, above which the states of continuum merge with σ* bands (band structure from [30]).

The π bonding and anti-bonding dispersion relations can be found from a 1-orbital tight-binding calculation [31]:

$$E_{g2D}\left(k_x, k_y\right) = \pm\gamma_0\left[1 + 4Cos\left(\frac{\sqrt{3}k_x a}{2}\right)Cos\left(\frac{k_y a}{2}\right) + 4Cos^2\left(\frac{k_y a}{2}\right)\right]^{1/2} \qquad (1.4.1)$$

where γ_0 is called the transfer integral. A similar 4-orbital tight-binding calculation gives the σ bands in Figure 1.7 [31].

Upon folding of the graphene sheet, the reciprocal lattice vectors K_2 along the nanotube and K_1 in circumferential direction satisfy the Periodic Boundary Conditions (PBC):

$$C_h.K_1 = 2\pi, C_h.K_2 = 0, T.K_1 = 0, T.K_2 = 2\pi \qquad (1.4.2)$$

which give the expressions:

$$K_1 = \frac{1}{N}\left(-t_2 b_1 + t_1 b_2\right), K_2 = \frac{1}{N}\left(n_2 b_1 - n_1 b_2\right) \qquad (1.4.3)$$

Since K_1 corresponds to circumferential periodicity, it is quantized: it can take the

values mK_1 where $m = 0,1,\ldots,N\text{-}1$, which gives rise to N discrete k vectors. The Brillouin zone is along K_2 with the length $2\pi/T$. The situation is illustrated in Fig. 1.8.

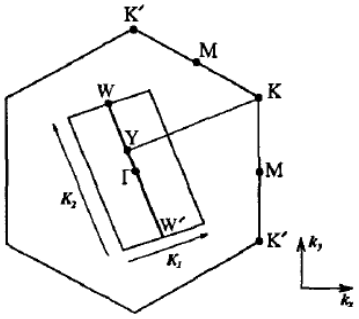

Figure 1.8 Brillouin zone of graphene (the area of the hexagon) and of nanotube (segment WW') and reciprocal lattice vectors of the nanotube (K_1 and K_2) (from [31]).

From Fig. 1.8, one concludes that since the gap closes at K-point in graphene BZ, when YK is an integer multiple of K_1, the nanotube will be metallic. It is not difficult to show that $\overrightarrow{YK} = \frac{2n_1 + n_2}{3} K_1$. Therefore when $(2n_1+n_2)$ or equivalently, $(n_1\text{-}n_2)$ is a multiple of 3, the tube is metallic.

From the 2D band structure of graphene, the 1D band structure of the nanotube will be obtained:

$$E_m(k) = E_{2D}\left(k\frac{K_2}{|K_2|} + mK_1\right) \tag{1.4.4}$$

where $m = 0,1,\ldots,N-1, -\frac{\pi}{T} \le k \le \frac{\pi}{T}$

Using eqn. (1.4.1), one obtains the following expression for the (n,n) armchair nanotube bands:

$$E_m(k) = \pm\gamma_0\left[1 \pm 4Cos\left(\frac{m\pi}{n}\right)Cos\left(\frac{ka}{2}\right) + 4Cos^2\left(\frac{ka}{2}\right)\right]^{1/2} \tag{1.4.5}$$

where $m = 1, ..., 2n, -\frac{\pi}{a} \le k \le \frac{\pi}{a}$

and the following for (n,0) zigzag nanotubes:

$$E_m(k) = \pm\gamma_0 \left[1 \pm 4Cos\left(\frac{m\pi}{n}\right) Cos\left(\frac{\sqrt{3}ka}{2}\right) + 4Cos^2\left(\frac{ma}{n}\right) \right]^{1/2} \qquad (1.4.6)$$

where $m = 1, ..., 2n, -\frac{\pi}{\sqrt{3}a} \le k \le \frac{\pi}{\sqrt{3}a}$.

The band structures for some examples of armchair and zigzag tubes (both metallic and semi-conducting) are shown in Fig 1.9.

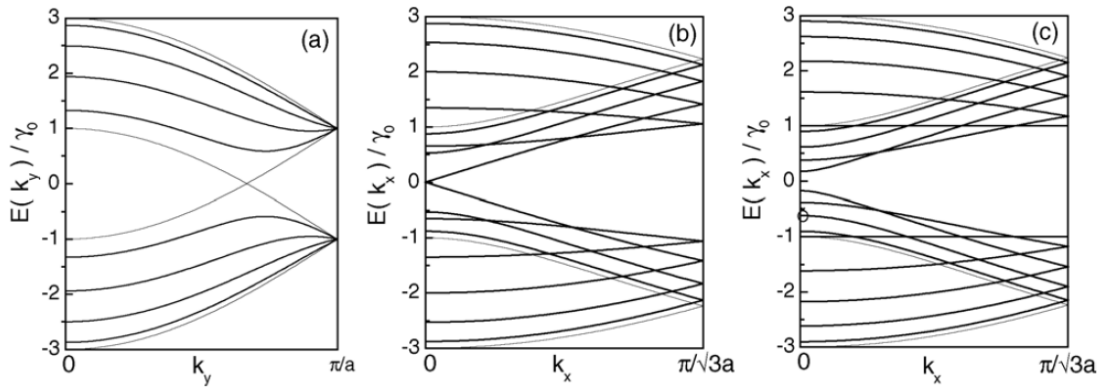

Figure 1.9 The band structure of a (a) (5,5) armchair, (b) (9,0) zigzag, and (c) (10,0) zigzag nanotube. (from [32]).

1.5 Non-Equilibrium Green's Function Formulation

The Green's function equation is as follows:

$$(ES - H)G = 1 \qquad (1.5.1)$$

where E is the (complex) energy, S is the overlap matrix, H is the Hamiltonian and G is the Green's function. This equation is written for each lead. The matrices can be broken to separate blocks corresponding to principal layers (PLs). A PL is the smallest block of the lead so that the interaction only exists between nearest neighboring blocks, i.e. the

Hamiltonian elements between the atomic orbitals that belong to two PLs that are not nearest neighbors are negligible. The Green's function equation will turn into an infinite number of equations. Generalizing steps described in Ref. [33] for non-orthogonal basis we obtain:

$$\begin{aligned}
&(ES_{00}-H_{00})G_{00}=1+(H_{01}-ES_{01})G_{10}\\
&(ES_{00}-H_{00})G_{10}=\left(H^{\dagger}{}_{01}-ES^{\dagger}{}_{01}\right)G_{00}+(H_{01}-ES_{01})G_{20}\\
&\vdots\\
&(ES_{00}-H_{00})G_{n0}=\left(H^{\dagger}{}_{01}-ES^{\dagger}{}_{01}\right)G_{n-1,0}+(H_{01}-ES_{01})G_{n+1,0}
\end{aligned} \tag{1.5.2}$$

We have used: $H_{00}=H_{11}=\cdots, H_{01}=H_{12}=\cdots$

and similar relations for overlap matrix. General term can be written:

$$\begin{aligned}
G_{n0}&=(ES_{00}-H_{00})^{-1}\left(\left(H^{\dagger}{}_{01}-ES^{\dagger}{}_{01}\right)G_{n-1,0}+(H_{01}-ES_{01})G_{n+1,0}\right)\\
&=t_0G_{n-1,0}+\tilde{t}_0G_{n+1,0}
\end{aligned} \tag{1.5.3}$$

Applying recursively, one obtains:

$$\begin{aligned}
&G_{n0}=t_iG_{n-2^i,0}+\tilde{t}_iG_{n+2^i,0}\\
&t_i=\left(1-t_{i-1}\tilde{t}_{i-1}-\tilde{t}_{i-1}t_{i-1}\right)^{-1}t_{i-1}{}^2\\
&\tilde{t}_i=\left(1-t_{i-1}\tilde{t}_{i-1}-\tilde{t}_{i-1}t_{i-1}\right)^{-1}\tilde{t}_{i-1}{}^2
\end{aligned} \tag{1.5.4}$$

We get:

$$\begin{aligned}
&G_{10}=t_0G_{00}+\tilde{t}_0G_{20}\\
&G_{20}=t_1G_{00}+\tilde{t}_1G_{40}\\
&\vdots\\
&G_{2^n0}=t_nG_{00}+\tilde{t}_nG_{2^{n+1}0}
\end{aligned} \tag{1.5.5}$$

Continue until $t_{n+1},\tilde{t}_{n+1}\le\varepsilon$.

G_{10} is then calculated:

$$G_{10}=\left(t_0+\tilde{t}_0t_1+\tilde{t}_0\tilde{t}_1t_2+\cdots+\tilde{t}_0\ldots\tilde{t}_{n-1}t_n\right)G_{00}=TG_{00} \tag{1.5.6}$$

where T is the transfer matrix. G_{00}, which is also called the surface Green's function, can now be calculated, using eqns.(1.5.2) and (1.5.6):

$$G_{S/D} = G_{00} = \left[ES_{00} - H_{00} - \left(H_{01} - ES_{01} \right) T \right]^{-1} \tag{1.5.7}$$

Using surface Green's function, one can obtain the source and drain self-energies:

$$\begin{aligned} \Sigma_S &= \left(H_{MS} - ES_{MS} \right) G_S \left(H_{SM} - ES_{SM} \right) \\ \Sigma_D &= \left(H_{MD} - ES_{MD} \right) G_D \left(H_{DM} - ES_{DM} \right) \end{aligned} \tag{1.5.8}$$

And then we can calculate the molecule's Green's function:

$$G = \left(ES_M - H_M - \Sigma_S - \Sigma_D \right)^{-1} \tag{1.5.9}$$

Transmission probability and the current are given by Landauer-Buttiker formula

$$\begin{aligned} T\left(E,V\right) &= Tr\left[\Gamma_D G \Gamma_S G^{\dagger} \right] \\ I &= \frac{2e}{h} \int_{-\infty}^{\infty} T(E,V) \left[f_S(E,V) - f_D(E,V) \right] dE \end{aligned} \tag{1.5.10}$$

where f_S and f_D are Fermi-Dirac functions for the source and the drain. The broadening matrices $\Gamma_{S,D}$ are given by [34-36]:

$$\Gamma_{D,S} = i\left(\Sigma_{D,S} - \Sigma_{D,S}^{\dagger} \right) \tag{1.5.11}$$

1.6 Density Functional Theory

Density functional theory (DFT) reduces the complicated many body problem of solving the Schrödinger equation for a few tens or hundreds atoms to the more manageable one particle problem of solving the Kohn-Sham (KS) equation:

$$\left[-\frac{1}{2}\nabla^2 + v_{ext}\left(r\right) + \int \frac{\rho\left(r'\right)}{\left|r - r'\right|} d^3 r' + v_{xc}\left(r\right) \right] \varphi_i\left(r\right) = \varepsilon_i \varphi_i\left(r\right) \tag{1.6.1}$$

where ρ is the electron density, $v_{ext}(r)$ is the potential due to ions, and $v_{xc}(r)$ is the so called exchange-correlation potential. All the many body complications are swept under

the rug in the exchange-correlation potential. The validity of this approach is proved in a theorem, the “Hohenberg-Kohn” theorem [37], which states that given a ground state density, it is possible to calculate the corresponding ground state wavefunction. This means that the ground state wavefunction, and consequently all the observables are functionals of the ground state density.

The KS equation should be solved self-consistently, i.e. obtaining the wavefunction that to some degree of accuracy gives the initial guessed density.

There are several choices for the exchange-correlation (*xc*) potential. In all choices, it can be written as sum of exchange and correlation terms. Local density approximation (LDA) is the simplest, assuming that the *xc* energy density (or e_{xc} defined as the integrand for the *xc* energy integral over space) is only a function of the density. Perdew-Zunger (PZ81, [38]) and Perdew-Wang (PW92, [39]) functionals are the most accurate ones. Generalized gradient approximation (GGA) is an approximation in which e_{xc} is assumed to be a function of density and its gradient. The most widely used examples are Perdew-Burke-Ernzerhof (PBE, [40]), and Becke-Lee-Yang-Parr, (BLYP, [41, 42]) functionals. The most accurate functionals for DFT calculations are hybrid functionals, where some combination of the exact form of exchange energy and some DFT approximation of exchange, plus correlation energy is used as *xc*. The most well-known example is B3LYP functional [43].

For geometry optimizations (or for dynamics), the Born-Oppenheimer approximation is used in which, the ions are treated classically, and the system is optimized to minimum ground state energy of the sum of the KS energy of electrons and the ion-ion interaction energy. For each step of optimization (i.e. moving the position of ions), the KS equation

must be solved self-consistently.

Chapter 2
The Boron Fullerenes

2.1 Introduction

Early Daedalus' musing on hollow carbon molecules [44], Osawa's carbon soccer ball structure [45], and the first Hückel calculation of stability of carbon fullerenes [46], all remained unsupported by experiment for almost two decades, until the discovery of the carbon buckyball, C_{60} [47]. Here we describe the structure, stability, and predict the existence of a round boron molecule B_{80}, which is very similar in shape and symmetry to the carbon fullerene C_{60} [48]. Besides the direct computations, the outstanding stability of the B_{80} buckyball is explained in terms of its particular construction, which consists of six double-ring clusters interwoven in a way to form a round hollow basket. B_{80} can also be viewed as a B_{60} (metastable in our calculations) polyhedron reinforced by extra atoms placed in the centers of all hexagons, to satisfy the Aufbau principle for boron-clusters composition [2].

Classical experiments and theories contains studies on small boron clusters [2, 21], most important of which appear to be the compact icosahedral B_{12}, and the family of boron double-rings (DRs) with various diameters. It is useful to view the B_{12} as a tight knot of six overlapping B_{10} DRs [see Fig. 2.1(a) (right)]. Most of the information in the literature is about boron clusters containing fewer than 36 atoms. In this study, we go beyond this to larger assemblies in order to explore if the reduction in the curvature might further lower the total energy and lead to yet more stable clusters. Of course the tremendous combinatorics of possible arrangements makes any exhaustive comparison

almost impossible. Instead we primarily sought the structures which combine several DRs of larger size (and lower strain) and yet remain not too sparse so that inter-ring bonding serves as an additional stabilizing factor. Indeed, the B_{80} emerged as a winner, with the largest cohesive energy compared to all others. The connection between the B_{80} cage and DR tubular clusters (some of which were already synthesized experimentally [4]) motivated us also to include here details of the DRs' energetics.

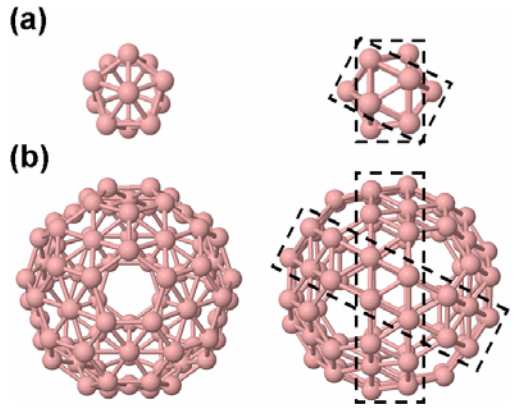

Figure 2.1 Optimized structures of B_{12} (a) and B_{80} (b) cages. Both structures are shown in front and side views. For the side views, the subgroup of atoms which form B_{10} and B_{30} DRs in B_{12} and B_{80} cages, respectively, are outlined.

2.2 Computational Method

The optimization of structures was performed within the density functional theory (DFT) framework, using generalized gradient approximation (GGA) for exchange and correlation functional PBE [40]. Results were obtained by allowing full relaxation of all atoms, using the plane-wave based Quantum-ESPRESSO package [49] and ultrasoft Vanderbilt pseudo-potentials [50]. The cutoff energy of 30 Ry for the plane-wave expansion and 210 Ry for the electronic charge density was found to be sufficient to obtain converged results. The Γ point was used for the Brillouin zone integrations in the case of the finite structures, and 1×1×16 (1×16×16) *k*-point sampling was used for the

one (two) dimensional infinite structures. The total energy was converged to 10^{-6} Ry and ionic positions were optimized until the forces acting on them were smaller than 10^{-3} Ry/Bohr. To study properties of finite structures, the super-cell geometry was taken to be a cubic cell with lattice constant sufficiently large to avoid interactions between the clusters (allowing at least 12 Å distance between clusters). For electronic structure properties and molecular orbital (MO) images GAUSSIAN03 package [51] was used in conjunction with GaussView molecular visualization software. For DR electronic structure calculations we used the PBEPBE method and all-electron 6-31G(d,p) basis set, to be consistent with the plane-wave results [52].

2.3 The Family of Boron Fullerenes and B_{80}

The properties of small boron clusters are better understood [2, 21]. Perhaps the central place among them belongs to B_{12} icosahedron which appears to be the building block of several known crystalline phases of bulk boron [2, 13]. In those phases, the B_{12} clusters are held together by directed bonds, either between atoms in adjacent clusters or via intermediate atoms. The most stable bulk structure containing B_{12} units is the α-rhombohedral boron [13]. The second in stability is the β-rhombohedral boron with the unit cell containing 105 atoms and the structure made up of a B_{84} super-cluster with I_h symmetry [13]. B_{84} cluster alone, however, is not stable and collapses if not supported in the lattice of the bulk, according to our calculations. Despite its importance, the B_{12} cage is not the most stable boron cluster composed of 12 atoms, since the most stable members of the B_n families with $n < 20$ are known to be planar [53].

Based on the structural similarities among larger boron clusters, a so-called Aufbau principle for boron clusters was conjectured by Ihsan Boustani [2]. According to this

principle, the most stable clusters can be constructed using two basic units: pentagonal pyramid B_6 and hexagonal pyramid B_7. In Fig. 2.1(a) we have shown the optimized B_{12} cage. As one can see from the figure, the B_{12} icosahedron is an example of a structure built from pentagonal B_6 units. In this study however, we look at the B_{12} cage from a different perspective, namely we consider its structure as built from staggered B_{10} DRs. In the right part of Fig. 2.1(a), the side view of the icosahedron shows clearly that B_{12} is built from crossing tubular B_{10} structures. The B_{10} structure consists of two pentagonal chains with a staggered arrangement of boron atoms. Each ring is rotated by an angle of $\pi/5$ with respect to the other in order to form the staggered configuration. Because B_{10} is the smallest stable DR structure made of boron atom, B_{12} is the smallest cage built completely from DR clusters.

In previous studies of the silicon cage clusters and tubes, their remarkable stabilization by insertion of transition metal atoms was observed [54]. Based on this observation, we tried to similarly stabilize the B_{60} fullerene cage by "reinforcing" each of its hexagonal facets by a transition metal atom, which appeared to be too big. When instead of transition metal, an extra boron atom was placed in each hexagon, the result was surprising. We found a structure, shown in Fig. 2.1(b), which is built up from 80 atoms, possesses unusually large cohesive energy (E_c, or E_{coh} in Fig. 2.3), preserves I_h symmetry (see Chapter 3 for more careful analysis of the symmetry), and is very stable according to our calculations. In addition, B_{80} has similar characteristics to B_{12} because it is built from DRs. In Fig. 2.1(b) (right), we mark two crossing B_{30} DRs that are constituents of the cage. The whole cage is made up of 3 such pairs (6 DRs in total).

The staggered configuration of each DR is formed by two rings with 15 atoms and each ring is rotated by an angle of $\pi/15$ with respect to the other.

The B_{80} cage is symmetrically similar to the C_{60} structure (see chapter 3 for more elaborate discussion of the symmetry of B_{80}). The only difference is the presence of an additional atom at the center of each hexagon. These facets of the B_{80} follow the Aufbau principle mentioned before although the hexagonal pyramid units here are rather planar.

In order to evaluate whether or not reinforcing pentagons (instead of or in addition to hexagons) would help with stability of the structure, we investigated two other cages; B_{72} and B_{92}, formed by placing extra boron atoms on top of pentagons (B_{72}) and on pentagons and hexagons (B_{92}) of the B_{60}. The structures are shown in Fig. 2.2(b) after optimization.

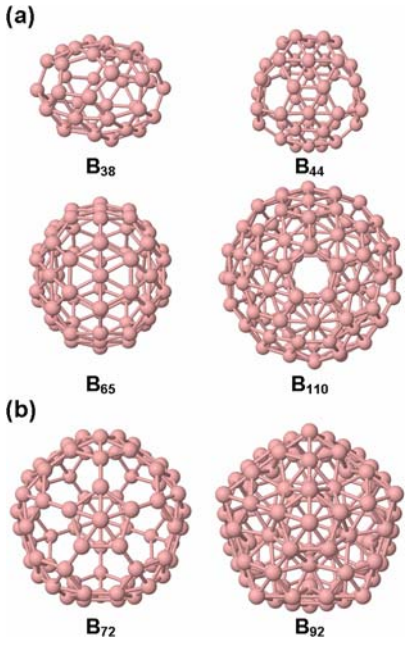

Figure 2.2 (a) Relaxed structures of other members of the family of boron cages with an additional atom at the center of each hexagon, which were found to be stable in our calculations. (b) B_{72} (left, with atoms at the centers of pentagons) and B_{92} (right, with atoms at the centers of hexagons and pentagons). B_{92} is very close in energy to B_{80}.

The B_{72} cage is round and preserves I_h symmetry but is less stable than the B_{80}. The B_{92} is completely built with triangular bonding units which are generally favorable in boron clusters [21], however, this cage is also less stable than the B_{80} cage.

This opens up the possibility of a completely new family of boron clusters, which may have similar shapes to carbon fullerenes but have an additional atom at the center of each hexagon. We studied this type of cages with sizes smaller than 80 atoms (derived from fullerenes with less than 60 atoms), as well as one bigger cage; B_{110}. More precisely, we applied reinforcement of hexagons to boron isomorphs of C_{24}, C_{26}, C_{28}, C_{32}, C_{36}, C_{50}, and C_{80} fullerenes (specified by D_6, D_{3h}, D_3, D_3, D_{6h}, D_{5h}, and I_h symmetries, respectively) and then optimized the obtained structures. Four of them were stable (for which, Wolfe conditions for convergence [55] were satisfied) and their relaxed structures are shown in Fig. 2.2(a). It is worth noting that none of these structures consist of DRs and perhaps for this reason, they do not have the exceptional cohesive energy that we observe for B_{80}. In Table 1 we summarized the values of E_c.

	symmetry	E_c (eV/atom)	HOMO-LUMO (eV)
B_{12}	I_h	5.01 (5.00)	0.737 (0.810)
B_{20}	I_h	4.74 (4.69)	1.253 (0.008)
B_{38}	D_3, *distorted*	5.47 (5.48)	0.935 (0.923)
B_{44}	D_{2h}, *distorted*	5.55 (5.56)	0.980 (0.965)
B_{60}	I_h	4.93 (4.91)	0.049 (0.050)
B_{65}	D_{5h}	5.69 (5.70)	0.095 (0.014)
B_{72}	I_h	5.60 (5.58)	0.269 (0.001)
B_{80}	I_h	5.76 (5.77)	1.006 (0.993)
B_{92}	I_h	5.72 (5.75)	1.129 (1.161)
B_{110}	I_h	5.73 (5.74)	0.119 (0.097)

Table 1 Symmetries, cohesive energies and HOMO-LUMO gaps of studied boron cages. The first values (for E_c and energy gap) correspond to results obtained with Quantum-ESPRESSO whereas the values in brackets were obtained using GAUSSIAN03.

In order to further verify the stability of B_{80}, we performed quantum molecular dynamics (MD) simulations at different temperatures (each run was 1.7 ps long). At temperature 700 K, the cage maintains its structure during the MD run and no significant deformations occur. At temperature 1000 K, it deforms but keeps its hollow construction.

Since we established the link between B_{12} and B_{80} cages on the one hand, and tubular DR clusters on the other, it is useful to compare their relative stability. In Fig. 2.3 we have plotted the cohesive energy of several DR structures versus the number of boron atoms (n). In the same figure we have also included the E_c values of all the cages mentioned above, as well as two fullerenes B_{20} and B_{60}. From Fig. 2.3 we can see that the E_c values of DRs monotonically increase from the value of 4.72 eV/atom for B_{10} to the value of 5.69 eV/atom for infinite DR (or strip, which is shown by the blue horizontal line), with the exemption of B_{32} and B_{34} DRs, which slightly break the monotonical behavior. Consequently, the most stable structure among all DRs is the strip. The red curve shows the $1/n^2$ behavior, based on the expected dependence of elastic strain energy on the DR diameter (which is proportional to n) [56].

Apart from the fact that DRs appear in the structure of B_{80}, we investigate their energies for yet another reason. Recent calculations show that DR B_n clusters with n = 20, 24, 32, and 36 are the most stable structures among all clusters with the same number of atoms [4, 18-20, 53]. Our results show that this is not the case for n = 80. B_{80} (E_c = 5.76 eV/atom) is not only more stable than the DR with 80 atoms (E_c = 5.66 eV/atom) but is also more stable than the strip (E_c = 5.69 eV/atom). The limit for the

stability of all boron structures is the α-rhombohedral bulk with E_c = 6.33 eV/atom (computed with the same method).

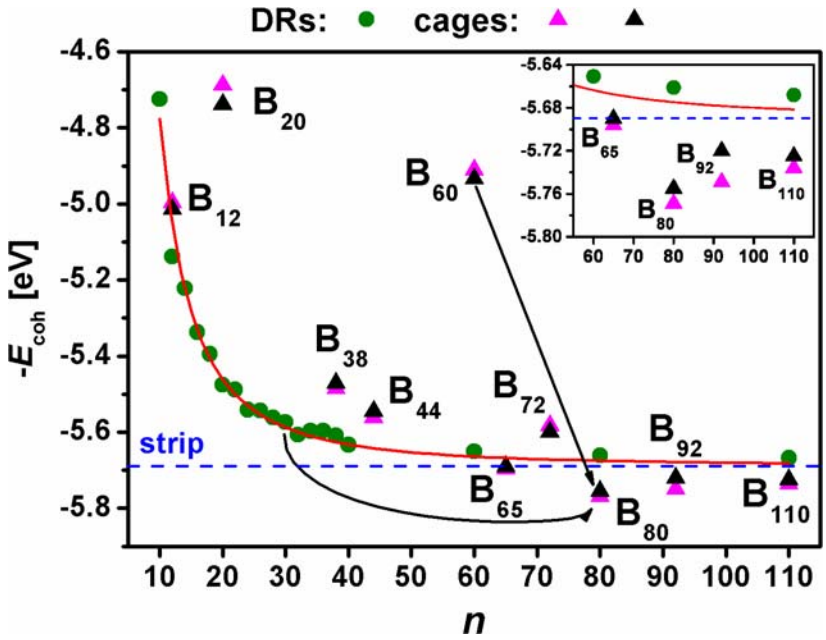

Figure 2.3 Negative cohesive energy ($-E_{coh}$)per atom as a function of the number of atoms n in the B_n clusters. The circles correspond to double-rings whereas the black (magenta) triangles correspond to cages calculated with Quantum-ESPRESSO (GAUSSIAN03). The blue horizontal line corresponds to the cohesive energy of the infinite double-ring (strip). The arrows show the increase in cohesive energy by reinforcement of hexagons (from B_{60} to B_{80}) and by appropriate crossing of the double-rings to form icosahedral structure (from B_{30} DR to B_{80}). The inset shows relative $-E_{coh}$ values for four cages B_{65}, B_{80}, B_{92}, and B_{110}, more pronouncedly.

To complete the description of the studied boron cages, it is important to analyze their structural and electronic properties. In the case of B_{60}, all nearest neighbor distances (l_{BB}) are the same (within 5×10^{-3} Å), with an average value of l_{BB} = 1.689 Å. The picture for B_{80} is, however, similar to that of the well known C_{60}: there are 60 longer (l_{ph} = 1. 727 Å) and 30 shorter (l_{hh} = 1.677 Å) bonds. In addition, there is a third group of 120 bonds (not present in C_{60}) between each atom at the center of each hexagon and its 6 nearest-neighbors (l_{BB} = 1.703 Å). The B_{60} and B_{80} cages have

approximately the same diameter d = 8.17 Å which is much larger than the diameter for C_{60} (d = 6.83 Å).

The HOMO-LUMO energy separation for all different clusters studied here, are listed in Table 1. The HOMO and LUMO of B_{80} are five-fold and three-fold degenerate with H_u and T_{1u} symmetries, respectively (both are odd under parity). The observation that can be made here is that the gaps exhibit alternations (as a function of the number of boron atoms) similar to that known for metallic clusters [57]. When the degenerate states (states belonging to the same irreducible representation of the point group) are partially occupied, the gap is small (B_{65} is an example of this case). But when they are fully occupied, the cluster exhibits considerably large HOMO-LUMO gap (which is the case for B_{80}).

Analysis and comparison of a number of boron structures presented in this work convincingly singles out the spheroid molecule B_{80} as an energetically favorable cage and therefore suggests that it is likely to appear as a result of self-assembly of boron atoms. Of course, specific conditions and kinetic paths to such an assembly cannot be derived from this analysis. What we show simply indicates its likelihood and suggests more careful search in experiments. There are no experimental reports about the existence of stable boron clusters with exactly 80 atoms. However there are two facts related to this topic that should be mentioned. In the context of an investigation for the crystal structure of YB_{66}-type boron-rich solids, Higashi *et al*. [58] proposed that YB_{66} contain non-icosahedral B_{80} units with about 50% of the boron sites randomly occupied; however the structure of those units has not been well established. There are also mass spectroscopy studies of boron-rich glasses [59, 60], which clearly display peaks in the

mass spectrum at the value 865 amu. These peaks could potentially correspond to clusters with 80 boron atoms, but the authors did not suggest such interpretation.

If the inorganic B_{80} cage is confirmed experimentally, it would be the second example in nature (after C_{60}), with a round, mono-elemental, and distinct hollow structure.

Chapter 3
Symmetry, Electronic and Vibrational Properties of the Boron Buckyball

3.1 Introduction

B_{80}, while essentially icosahedral looking in shape, it has different isomers, all close in energy and geometry, with symmetries such as I_h, T_h, and C_1 [61, 62]. Fig. 3.1 shows the total electron density image of this molecule. We should also mention that boron clusters in general have had application in cancer therapy for years [22].

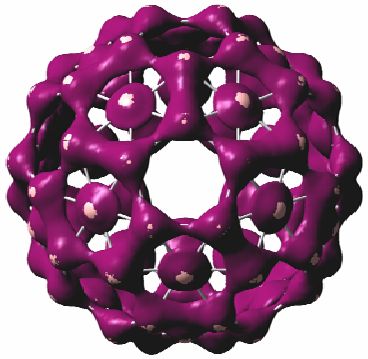

Figure 3.1 The B_{80} total electron density (Gaussian isovalue = 0.128).

B_{80} (like C_{60}), can be imagined as sheet wrapped on sphere [63]. The most stable structure for the sheet, the α-sheet, was recently reported [64, 65] (Fig. 3.2). B_{80} can be viewed as wrapped α-sheet on a sphere: "empty" hexagons are replaced by 12 pentagonal disclinations required topologically, and strips enclosing them are replaced by B_{30} DRs. Fig. 3.2(a) shows how the sheet can be folded to form a pentagonal disclination. Fig. 3.2(b) highlights the un-folded B_{80} molecule on an α-sheet. If α-sheet

is indeed the most stable structure for the sheet, it should be more stable than any hollow ball and nanotube [65-67] (because of curvature strain energy), and among quasi-planar structures (because of surface energy). B_{80} as the smallest possible spherically wrapped α-sheet cage has a special place in the first category above (hollow balls). Solid boron clusters might also have comparable stability as being cut from the bulk, which is more stable than the sheet (α-bulk for instance is 0.4 eV/atom more stable than α-sheet). Recently it was reported that some stuffed boron fullerenes were more stable than B_{80} [68, 69].

Here we study the symmetry, electronic structure, and vibrational modes of different isomers of B_{80} [70]. We also discuss its precursor, i.e. sheet. We review different stable geometries of sheet and compare the corresponding cohesive energies to that of B_{80}.

3.2 Methodology

The methods used are the same as described in chapter 2. For careful analysis of energy and electronic structure of different isomers of B_{80}, optimizations were made using a more accurate B3LYP/6-31G(d) method, and for frequency calculation, due to heavy computational demand, we used the same method but minimal basis set STO-3G.

We start by looking into structure that is precursor to B_{80}, i.e. boron sheet.

3.3 Boron Sheet

Until recently, the most stable structure for the sheet was believed to be triangular. Flat triangular sheet turns out to be meta-stable. Triangular boron sheet becomes puckered [71, 72]. Fig. 3.3 shows the construction of this sheet. The values for cohesive energy (E_c), bond lengths (l_1 and l_2), and off-plane distance are summarized in Table 2.

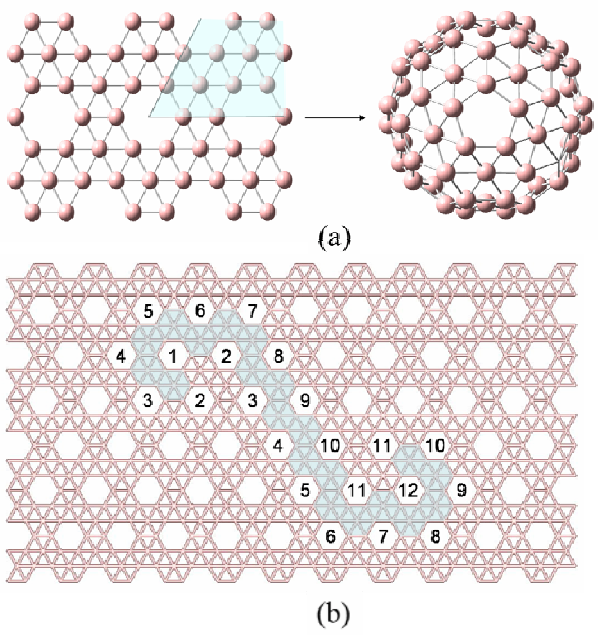

Figure 3.2 (a) Atoms in shaded area of the α-sheet (left) are removed and the ones on the lines are identified to form pentagonal disclination in B_{80} (right). Figure shows only half of the molecule. (b) Projection of B_{80} on α-sheet. Numbered facets represent the pentagons in B_{80}.

These values are based on our GGA results (using Quantum-ESPRESSO), which are in good agreement with previous reports [71, 72]. In both cases (puckered and flat) the sheet is metallic, with no energy gap in the band structure.

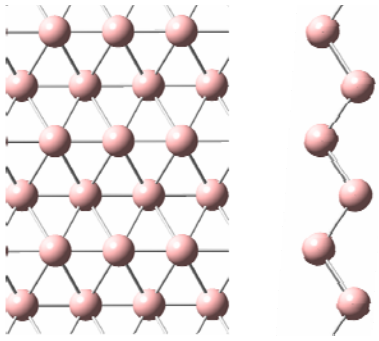

Figure 3.3 Top-view (left) and side-view (right) of the stable triangular boron sheet (puckered).

	E_c (eV/atom)	***l_1*** (Å)	***l_2*** (Å)	**Off-plane distance** (Å)
Flat	5.62	1.70	1.70	0.0
Puckered	5.84	1.62	1.88	0.925
α-sheet	5.93	1.70	1.70	0.0

Table 2 Cohesive energy (E_c), first nearest neighbor bond length (l_1, horizontal in Fig. 3.2 (α-sheet) and 3.3 (triangular sheet)), Second nearest neighbor bond length (l_2, diagonal), and the off-plane distance (projection of the l_2 bonds on the axis normal to the sheet)

Looking at the triangular lattice as super-positioned honey-comb (graphene-like) lattice + centers, it was shown recently that removing 1/3 of central atoms can further strengthen the triangular units and help with stability [64]. The resulting structure, the α-sheet (Fig. 3.2), is flat and metallic. Its values for bond length and cohesive energy obtained by GGA method are given in Table 2.

The B_{80} cohesive energy (5.76 eV, using the same method [48]) is below the corresponding value for α-sheet (5.93 eV), due to curvature strain energy.

3.4 B_{80}

3.4.1 Symmetry

It was already mentioned in the introduction that there are various isomers of boron buckyball, close to each other in energy and structure. Here we consider three B_{80} isomers obtained by B3LYP/6-31G(d) structural optimizations. Visually their geometries are almost identical [61], however, a detailed analysis reveals important differences in their symmetries. Namely, two out of three structures under consideration are very close to having icosahedral (I_h) and tetrahedral (T_h) symmetries, while the third one appears to have no symmetry at all (C_1). Correspondingly, we denote these B_{80}

isomers as I_h, T_h, and C_1. All the optimizations were performed without any symmetry restrictions, and our structures correspond to the true local minima of potential energy surface. The I_h isomer lies lowest; with total energy 3.6 meV lower than T_h and 30.3 meV lower than C_1 (the total energy differences are clearly very small and are sensitive to the method).

To estimate the deviations of I_h and T_h isomers from the corresponding ideal symmetries, let us consider the values of the dihedral angle between the six-membered ring and the plane formed by two of its atoms with the central boron atom. For the I_h isomer, the dihedral angles are from 3.26° to 3.81° (towards the center of the buckyball), i.e. their deviation from the average is negligible (less than 0.3°). In the case of the T_h structure, there is one group of eight central atoms with dihedral angles of 8.88° to 9.07° towards the center, and another group of twelve central atoms with small (~ 1°) dihedral angles away from the center. Our T_h isomer is similar to the "isomer A" of Ref. [62]; one can see this reference for the description of its geometry. For comparison, the dihedral angles in the C_1 isomer vary from 7.54° towards the buckyball center to 1° away from it.

The symmetry is also reflected in electron charge transfer from central boron atoms to the B_{60} skeleton [61]. The amount of Mulliken charge transfer is 0.149 e to 0.154 e in I_h case, 0.063 e to 0.065 e for the group of 8 atoms and 0.232 e to 0.233 e for the group of 12 atoms in T_h case, and in the range of 0.074 e to 0.205 e in C_1 case (Fig. 3.4). Finally, the symmetry of the B_{80} isomers under consideration is further confirmed by the analysis of their electronic structure.

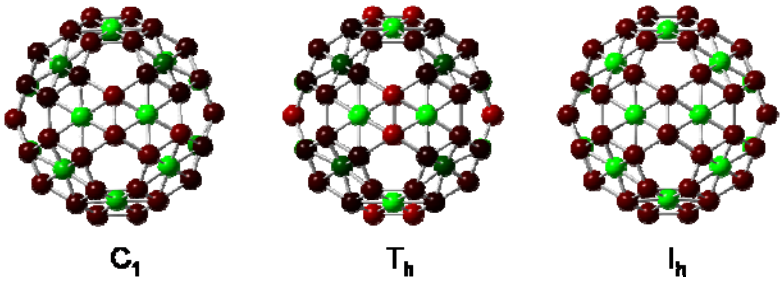

Figure 3.4 Visually the geometries of structures are almost identical, yet one can see different symmetries from the charge redistribution. Mulliken charges are shown for the three isomers C_1, T_h, and I_h. Green (red) shows positive (negative) atomic charges. The brighter green corresponds to more positive charge and smaller dihedral angle.

3.4.2 Electronic Structure

There are a total of 200 occupied MOs in B_{80}. It is helpful to think of them as the linear combinations of the boron atomic orbitals (AOs), and to distinguish between the AOs belonging to the two non-equivalent groups of boron atoms, namely, the twenty atoms situated in the centers of hexagons and the sixty other atoms forming a structure analogous to C_{60}.

The lowest 80 MOs are linear combinations of 1s-AOs of boron atoms, with a negligible contribution of higher AOs. The twenty boron atoms in the centers of hexagons mainly contribute to the MOs 1-20, which have very close energies; the other sixty atoms mainly contribute to the MOs 21-80, which are also nearly degenerate.

The higher occupied MOs of B_{80} are mostly made of boron 2s- and 2p-AOs and can have either σ or π character. There are only 60 π-electrons in the structure (which can be thought of as donated by the sixty equivalent boron atoms), and correspondingly, 30 π-orbitals are occupied.

Molecular orbitals of a nearly-spherical molecule can be well approximated by the spherical harmonics [73, 74], and thus strongly resemble AOs of various types. The

MOs having the azimuthal quantum number L = 0, 1, 2, 3, 4, 5, 6, etc., are commonly designated as S, P, D, F, G, H, I, etc., orbitals, analogous to the standard AO naming.

As the frontier molecular orbitals of B_{80} are of π-type, we concentrate on the π-MOs. Their energies for three isomers with C_1, T_h, and I_h symmetries are shown in Fig. 3.5. One may compare this energy diagram with that of C_{60} [73]. Notice that the numbers of occupied π-orbitals in C_{60} and B_{80} both equal 30 and thus do not satisfy the $2(N+1)^2$ Hirsch aromaticity rule [75], because the H shell (L=5) is not filled completely.

The rightmost column in Fig. 3.5 shows the spatial distribution of one typical molecular orbital for each quantum number L [76]. The orbital degeneracy is determined by the azimuthal quantum number L and the symmetry of the molecule under consideration. For example, the five-fold degenerate d-type atomic orbitals of transition metals split into a triplet and a doublet in the octahedral crystal field (see e.g., Ref. [77]). Similarly, lowering the isomer symmetry from I_h to T_h leads to the orbital splitting, clear for instance for HOMO (MOs #196-200, H-type) in Fig. 3.5. In particular, the symmetries of structures are reflected in their HOMO degeneracy: it is 5-fold for I_h (within 5 meV), 3-fold for T_h (within 2 meV), and nondegenerate for C_1. For the two symmetrical isomers, T_h and I_h, the representations of their symmetry groups are shown for all the π-type molecular orbitals in Fig. 3.5.

Since the symmetric (I_h) structure has a non-degenerate ground state (HOMO is fully filled), the break of symmetry in other isomers is not due to Jahn-Teller.

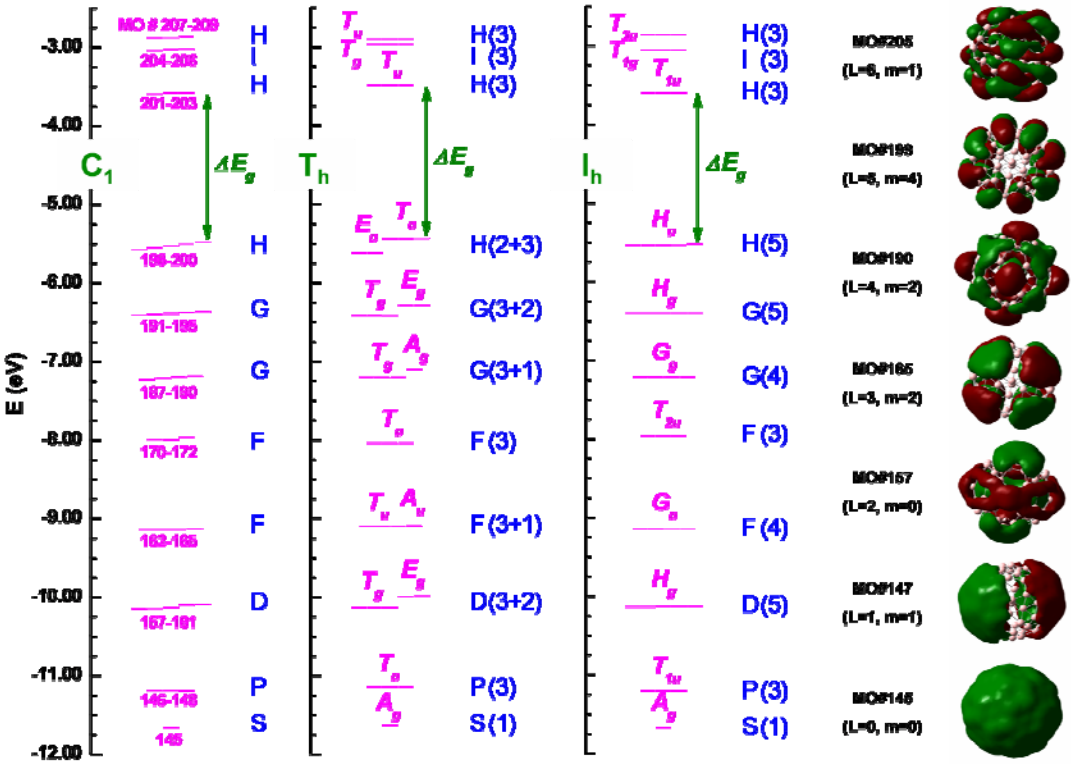

Figure 3.5 Energy diagram showing the π-type molecular orbitals of different isomers of B_{80}, calculated with B3LYP/6-31G(d) method/basis. The left, middle, and right diagrams correspond to C_1, T_h and I_h isomers, respectively. The levels with energy difference less than 10 meV are considered degenerate. The green arrow marks the HOMO-LUMO gap (ΔE_g = 1.88, 1.95, 1.93 eV for C_1, T_h and I_h, respectively). For the energy levels of T_h and I_h structures, the corresponding representations are shown. For each type of spherical harmonics (S, P, D, etc.), the spatial distribution of one typical molecular orbital is shown in the right column (Gaussian isovalue = 0.01).

3.4.3 Vibrational Modes

To analyze the vibrational modes of boron buckyball, we used B3LYP/STO-3G method/basis [51] because of the computational burden. The B_{80} geometry used for this analysis was relaxed using the same method, which has T_h symmetry (close to "isomer B" of Ref. [62], with 12 (8) central atoms making dihedral angle ~ 12.5° (8°) towards (away from) the center). B_{80} has 64 distinct intramolecular mode frequencies in the range of 154 cm^{-1} for radial vibrations to 1181 cm^{-1} for tangential ones. The low lying

frequencies correspond to the central atom vibrations, which shows that their off-plane movement is soft mode.

The breathing mode frequency is 474 cm^{-1}. In this mode, the 12 central hexagonal atoms with dihedral angle towards the center move in opposite phase with respect to the rest of the atoms. It is worth noting that in the Raman spectrum reported for BT samples [5], there is a peak close to this value of frequency (~420 cm^{-1}). The authors also attribute the peaks at the range of 400 cm^{-1} to 600 cm^{-1} to either smaller diameter BTs or to other boron structures present in the sample [5].

3.5 Conclusion

We briefly reviewed the energetics and structure of boron sheet in order to compare its cohesive energy to that of the B_{80} (which can be considered as the sheet wrapped on sphere). We also investigated the geometry and electronic structure of double-rings to some detail, since they have special place in boron chemistry. At last we examined the B_{80} from MO energy level and symmetry point of view, as well as frequency modes. Analysis reveals that there are several minima around icosahedral structure. Existence of different isomers close in energy to original structure further lowers the free energy at some appropriate temperature. This will help in self-assembly of the atoms by increasing entropy and favoring the path to lowest free energy, which increases the likelihood of experimentally detecting B_{80} (since these different isomers' energies all lay within thermal fluctuations at room temperature).

Chapter 4
Probing Properties of Boron α-tubes by *ab initio* Calculations

4.1 Introduction

Boron clusters of different shapes [2, 4, 19-21], including nanometer-wide tubes [2, 3, 5, 18, 71, 78, 79], have attracted attention of researchers for some years. Most recently, two theoretical observations have stimulated further focused interest to the field. One was the finding that boron can form rather stable hollow *spheres* similar to the well known carbon fullerenes, including B_{65}, B_{92}, B_{110}, and particularly the boron buckyball B_{80} [48]. Another important observation was that among the different possible 2D-*planar* assemblies of boron atoms, one particular pattern called α-sheet [64, 80] ensures the best occupancy of the bands by electrons and therefore has the lowest total energy. In different ways, both B_{80} and the α-sheet can be viewed as precursors for the boron tubes (BT), and suggest specific structure of the nanotube wall which previously remained a subject of debate [2, 71, 72, 78]. Indeed, B_{80} can be "stretched" into a tube by a sequence of insertions of the equatorial rings [63, 81], as was often discussed in establishing connection between the carbon fullerenes and nanotubes. In this case a hemisphere of B_{80} or a larger fullerene naturally serves as possible closure cap to the tube, Fig. 4.1a-c. Unfolding such uncapped cylinder yields exactly the α-sheet pattern, with the boron atoms missing at the right sites of the triangular lattice, Fig. 4.1c→d. Inversely, one can start from the α-sheet as common precursor and wrap it into a fullerene sphere, with the twelve appropriate 60° wedge-cutouts creating the pentagonal

disclinations, Fig. 4.1d→a. Yet more straightforward, the sheet [64, 80] can be folded into a boron tube of a desired chiral twist and diameter (Fig. 4.1d→c). One should point out that such "precursors" considerations are instructive from theoretical point of view but have little to do with possible synthetic routes.

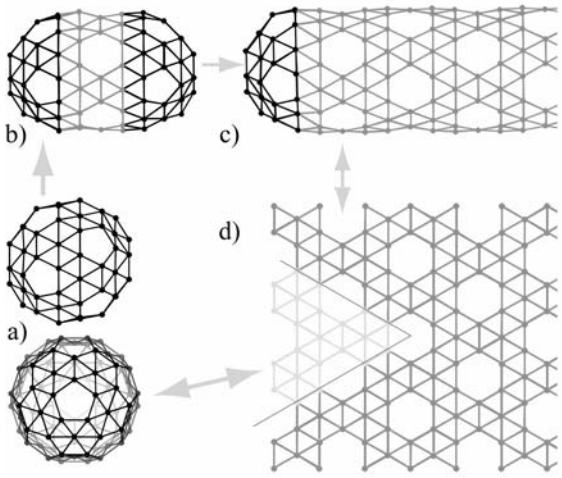

Figure 4.1 Schematics of interrelation between the B_{80} (a), which can be extended into prolonged cages like B_{120} (b) and further to nanotubes (c) by sequential insertion of the additional rings. Tube in turn can be unfolded into α-sheet (d). The shaded area in (d) marks the cut out for pentagonal disclinations when folding a sheet into B_{80} sphere.

Demonstrated preferred stability of the α-sheet [64] suggests that the tube obtained by wrapping its strip and reconnecting the covalent bonds, should also be more stable than others, with the binding energy just slightly less than the sheet, due to the elastic strain of curvature. At the same time, electronic structure of such α-tubes originating from the metallic sheet, is expected to remain metallic [64, 80] (previously discussed other BT are also believed to be metallic [18, 71, 72]) irrespective of diameter and chirality, as opposed to carbon nanotubes (CNT), which could be both metallic and semiconducting [82]. Such unvarying metallicity, if confirmed, could be a great benefit,

compared to the mixed types of the hard to separate CNT (separation remains a challenging task, which plagues the applications). Therefore, the prospect of having only metallic BT is considered as great advantage over CNT [5, 18, 72, 78], On the other hand, a lack of semiconductors among the BT could limit their applications in electronics, sensing, opto-electronics, etc.

Nanotubes	Diameter (Å)	C (N/m)	ν	f_{RBM} (cm^{-1})
(5,5)	8.13	209.4	0.18	238.9
(9,0)	8.63	206.7	0.21	224.8
(6,6)	9.93	202.1	0.26	195.9
(12,0)	11.31	204.6	0.21	170.6
(7,7)	11.37	215.2	0.20	173.7
(8,8)	13.13	214.0	0.21	150.2
(18,0)	16.50	217.5	0.15	119.2

Table 3 Calculated stiffness (C), Poission ratio (ν), and radial breathing mode frequencies (f_{RBM}) of boron α-tubes.

Here we use *ab initio* calculations to verify that the boron α-tubes are stable, with the binding energy very close to that of the sheets [66]. We further assess their mechanical stability in response to small deformations, calculate the basic stiffness constants, and find them to be comparable to the well studied and somewhat stronger CNT and BNT (boron-nitride tubes) [83-88]. Based on this, the radial breathing mode frequency, detectable by Raman spectroscopy and often used as a signature for hollow tubes, can be computed for arbitrary α-tubes. In spite of their overall stability, we observe that the cylindrical curvature causes a degree of buckling, with specific boron atoms departing from their in-plane positions. This buckling appears to have profound effect on the electronic structure. The tubes with the smaller diameters are semiconducting, while for $d \gtrsim 1.7$ nm they retain metallic no-gap characteristic of the α-sheet ($d = \infty$).

4.2 Methodology

The structural optimization for a set of nanotubes below is performed using projected augmented wave method with a plane wave basis set employing periodic boundary conditions and the conjugate gradient technique within the generalized gradient approximation (GGA) of PBE [89] for the exchange-correlation energy [90-93]. The cutoff energy for the plane wave expansion is taken to be 318 eV. The one dimensional Brillouin zones of different nanotubes are sampled by equivalent set of k-points, which are also sufficient to converge the energies. The structures are considered to be fully relaxed when the absolute value of the force on each ion becomes less than a 0.001 eV/Å; this strict criterion is important not to miss structural details such as atomic buckling. No less than 14 Å vacuum space is used in lateral directions to avoid any interactions between the periodic images of the nanotubes.

4.3 Structure

Calculating the α-sheet with the above described method yields the binding energy (E_b = 5.99 eV) and bond length (b = 1.67 Å) close to the values of Tang et al [64].

For naming purposes, we choose the indexing of the BT to correspond to the long-accepted convention for the CNT and BNT: with the two $\sqrt{3}\cdot$b-long basis vectors 60° apart, each directed along the zigzag motif in the lattice, the tube circumference is specified as a pair of components (n,m). This implies that any (n,m) tube derived from α-sheet exists only when (n – m) is a multiple of three. The diameter of the (n,m) tubes can be given by the formula $d = 0.94\sqrt{n^2 + m^2 + nm}$, Å. In order to explore the mechanical and electronic properties of the α-BT somewhat comprehensively, we consider both armchair and zigzag types, Table 3. We choose three zigzag BT to cover a

reasonable range of diameters which can reveal the common physics, with indexes (9,0), (12,0), and (18,0). For the armchair BT, we study four nanotubes with varying indexes and diameters, (5,5), (6,6), (7,7) and (8,8). We find that relaxation is very much diameter dependent, and occurs mostly around the filled hexagons, where the central boron atom B_c is inserted, relative to a hexagon tiling of graphene type. Generally, these central B_c atoms buckle inwards by departing off the plane of the hexagons, Fig. 4.2c (inset). Not all the central B_c-atoms buckle, but this rather happens in every other filled hexagon. With the increasing diameter, the center-atoms B_c systematically move back into plane of the hexagons, Fig. 4.2c. This mode of geometrical relaxation appears to have important effect on the electronic structure of the nanotubes, as discussed later.

4.4 Mechanical Properties

In order to be practically realizable and possibly useful in applications, the nanotubes should be able to stand some mechanical deformations. We evaluate the mechanical stiffness of the BT by calculating the in-plane stiffness C, the Poission

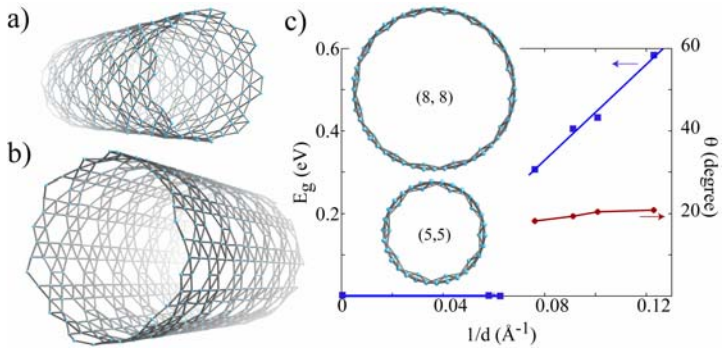

Figure 4.2 The relaxed structure of (a) armchair (8,8), and (b) zigzag (18,0) α-tubes. Plots (c) show the band gap E_g (left axis) and dihedral angle θ formed by the B_c atom and the plane of hexagon (right axis) versus curvature, 1/d. Axial view of (5,5) and (8,8) α-tubes illustrates the degree of atomic buckling, inset in (c).

ratio ν, and the flexural rigidity D of their wall (The hexagonal symmetry of two-dimensional lattice of α-sheet ensures its isotropic elastic properties and thus allows one to replace the atomistic structure by the continuum shell model with appropriate parameters [94].) Computing the energy E per atom as a function of elongation ε under uniaxial tension yields the value of C = $\frac{1}{a}\frac{\partial^2 E}{\partial \varepsilon^2}$, where a is the area per atom in the α-sheet. The Poisson ratio ν can be evaluated from the ratio of relative reduction of the diameter $\varepsilon_\perp$ and the axial strain ε. Fig. 4.3a shows one such example of calculation of C for (8,8) armchair BT, where energy per atom as a function of elongation strain ε is plotted and fitted to a parabola, ~½Cε^2. We also show within the same graph the change of diameter with the elongation, which gives us the Poisson ratio. The values for C and ν for all considered BT are given in Table 3. The overall variation in the values of C is within 8% of an approximate value C = 210 N/m. The values of ν around 0.2 show similar variation.

In addition to in-plane stiffness C, the value of flexural rigidity D can be defined as a coefficient in the energy of unloaded/free relaxed tubule as a function of its diameter d, E_b = const + 2D/d^2, where E_b is the equilibrium binding energy/atom of the tubule. The flexural rigidity gives the dependence of the energy on the curvature of a 2D sheet. Since both zigzag and armchair BT are formed by wrapping of the same α-sheet, this value should be similar for both. In Fig. 4.3b we plot the strain energy per atom as a function of curvature, and the data fits well to a straight line whose intercept with y-axis gives the E_b = 5.99 eV/atom of the α-sheet. The half of the slope of this line gives the value of D = 1.82 eV Å^2. Thus the resistance to mechanical deformation for BT is quite high (within 60% of CNT parameters [83, 86]). Knowledge of C and D constants permit

to rather fully characterize the elastic mechanical behavior of the BT. For example, another important measure of stiffness is so called persistence length [95] l_p (a correlation length for the direction of a tube exposed to equilibrium fluctuations at temperature T). Its magnitude is proportional to the tube stiffness, $l_p = \pi C d^3/8k_bT$ and amounts to fraction of millimeter at room temperature for the typical nanometer diameters. Such structures would not only be able to sustain some incidental strain but may also be used for some mechanical applications.

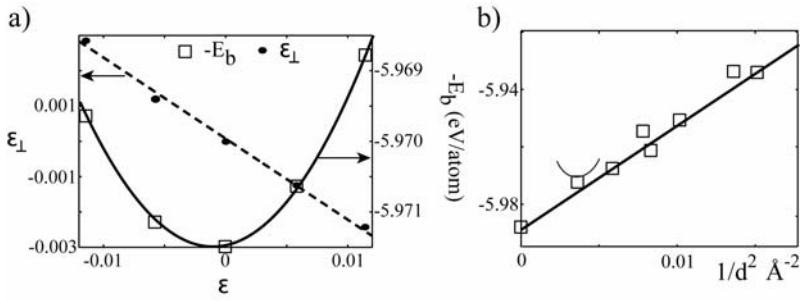

Figure 4.3 (a) Square parabola of the energy per atom with the axial strain ε, here for (8,8) tube, is used to compute the wall in-plane stiffness C for the α-tubes. The straight line shows the radial reduction $\varepsilon_\perp$ versus tensile strain ε, to yield the Poisson ratio, ν. (b) Plot of $E_b(d)$ versus square of the inverse diameter of BT. The intercept of this curve with y-axis gives the binding energy for the α-sheet, which agrees well with directly computed $E_b(\infty) = 5.99$ eV/atom.

4.5 Radial Breathing Mode

Furthermore, knowledge of the shell parameters allows one to calculate some vibrational frequencies without embarking into full analysis of all molecular vibration modes. Of particular interest for identification of hollow structures is the radial breathing mode (RBM) frequency f_{RBM}. It can be easily obtained as $f_{RBM} = \frac{1}{\pi c d}\sqrt{\frac{C}{(1-\nu^2)\rho_s}}$, where ρ_s is the mass density of the sheet, per unit area. (The

speed of light *c* is to convert to spectroscopic cm^{-1} units.) The values for f_{RBM} are given in Table 3, and can be generally estimated as $f_{RBM} \approx 210$ nm/d, cm^{-1}. Extrapolating to the d = 3 nm yields the breathing mode frequency near 70 cm^{-1}. This differs from the breathing mode frequency detected in the Raman spectra [5], which may indicate some underlying difference in the actual structures. (Note that the corresponding value for CNT is 76 cm^{-1}, based on well established parameters for carbon [56, 96])

4.6 Electronic Structure

Turning to the electronic properties of these nanotubes, we find that all the zigzag and armchair nanotubes with smaller diameters are semiconducting, Fig. 4.4a and d. While the sheet is originally metallic, in cylindrical BT large enough curvature and consequential buckling do open the gap. The gaps in armchair nanotubes are indirect and lie within the range of ~0.6 eV, Fig. 4.2c. Indeed, one can analyze the origin of this unexpected gap opening by calculating the band structure of *unrelaxed* armchair BT. In this case, they remain metallic, Fig. 4.4c. On the other hand, when fully *relaxed*, same nanotubes become semiconducting, Fig. 4.4d. To further clarify the role of buckled B_c atoms, we have analyzed the band-decomposed charge densities of the valence band maximum (VBM) of relaxed, and unrelaxed (8,8) BT (example plotted in Fig. 4.4e, and f for VBM of unrelaxed and relaxed tubes, respectively). One can see that the charge density of the VBM originates from the buckled B_c-atoms and their nearest neighbors. In the Fig. 4.4e and f, we can clearly see the effect of rehybridization on the B_c-atoms induced by the buckling, in terms of the change in the contribution from those atoms to the electron density. Since this buckling does not break the symmetry of the nanotubes, opening of the gap should not be attributed to Jahn-Teller type of distortions, but

appears to be due to rehybridization. As the dihedral angle formed by the B_c-atom and the plane of the hexagon decreases (Fig. 4.2c), the nanotube eventually transforms into metal. We have explicitly verified this by performing calculations on few selected armchair and zigzag tubes with the larger diameter [e.g. (10, 10), (11, 11), (21, 0), and (24, 0)].

Owing to the metallic nature of α-sheet, this transition to metal is very much expected. The band structure of a (21, 0) BT is shown in Fig. 4.4b, where several bands visibly cross at the Γ-point. This is because Γ-point of the zigzag BT coincides with that of the sheet, unlike armchair BT. These bands are highly dispersive implying that the effective mass of the charge carriers should be very small, leading to high mobility and better conductivity. There are several bands in the vicinity of the Fermi level, which also ensures the large carrier density. The metallicity of the larger diameter BT, low effective mass, high mobility, and conductivity qualify the BT as conductors at nanoscale and hence they could potentially be used as metallic interconnects in electronic devices.

4.7 Summary

In summary, we study the mechanical and electronic properties of pure boron nanotubes derived by wrapping the recently predicted as most stable α-sheet [64]. While stability of such α-tubes could be anticipated (being derived from a stable sheet), we do verify it by direct energy minimization. Calculations allow one to obtain the mechanical parameters of boron α-tubes such as stiffness $C \approx 210$ N/m, Poission ratio $\nu \approx 0.2$, and flexural rigidity $D \approx 1.8$ eV Å^2. We further show how the basic vibrational frequencies for the α-tubes can be calculated, with the Raman detectable radial breathing frequency as important example. We note that its computed value differs noticeably from the

reported based on Raman spectroscopy experiments [5]. The discrepancy may indicate that the actual BT have structure distinctly different from the α-tubes, or their stiffness

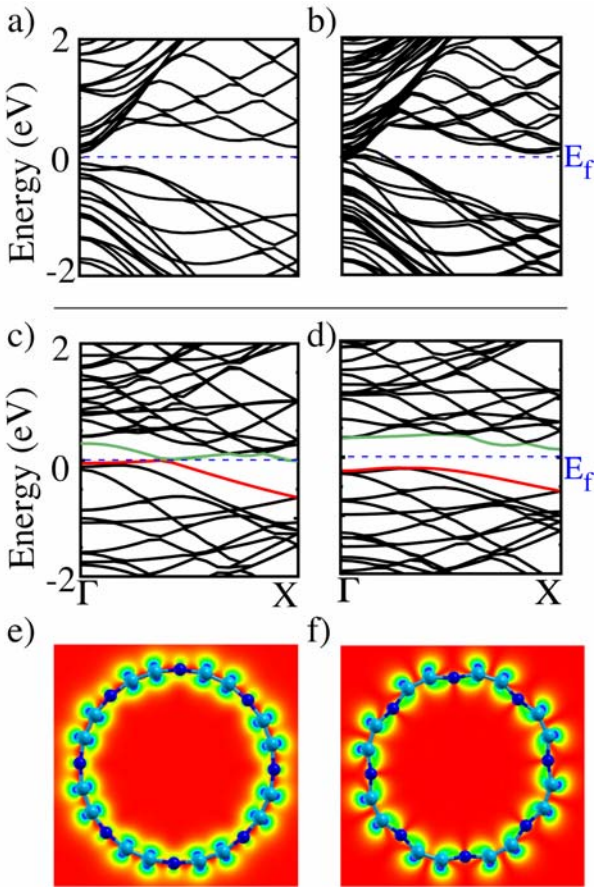

Figure 4.4 Band structure of (a) zigzag (18,0), (b) (21,0), (c) unrelaxed, and (d) relaxed armchair (8,8) tubes. Band-decomposed charge density in the plane perpendicular to the axis, for the highest occupied bands (e) for unrelaxed and (f) for relaxed (8,8) tube. The dark blue atoms are the central B_c-atoms, which buckle upon the relaxation.

in the sample is affected by additional lateral forces, and calls for future investigation of these structures. (In fact, one of the observed Raman peaks [5] is close to the RBM frequency of a B_{80}, 420 cm^{-1}). The α-tubes have a clear distinction in their electronic properties as the tubes of smaller diameters open the band gap and are semiconductors, according to our calculations. We relate the origin of semiconductor-gap in BT to the specific relaxation-buckling in atomic positions, which leads to rehybridization of the

orbitals. While the obtained mechanical properties appear rather robust and uniform among the tubes, further studies are necessary to determine the broader range of electronic properties, to include the chiral tubes as well. Nevertheless, the combination of emerging features makes boron α-tubes (BT) promising material for electronic, bio- and chemical sensing, and optical applications.

Chapter 5
Polymorphism of 2D Boron

5.1 Introduction

When it comes to its structural organization, elemental boron offers more puzzles than its close neighbors in the periodic table, ubiquitous carbon and silicon. At the large scale, boron displays multiple bulk phases [9, 97], while its smallest clusters are also diverse, as established experimentally and in theory [98, 99]. For larger nanostructures, even their possibility and basic makeup remain unsettled. Two-dimensional layers, nanotubes, or fullerene-type cages yield very scarce factual evidence [5, 100, 101] and remain a subject of ongoing debate. Recent prediction of the round boron molecule, B_{80}-buckyball [48], has ignited further interest. It was followed immediately by the proposals of stable two-dimensional boron, particularly appealing as graphene analog, and called α-sheet [102]. Inversely, the latter could be considered as a precursor foldable into B_{80}-sphere or a nanotube [66, 102].

B_{80} buckyball remained a subject of particular interest to theory, in part due to its similarity to celebrated C_{60}, and also as being contested regarding its symmetry [61, 62] and stability relative to other proposed hollow or filled isomers or larger clusters [69, 103, 104]. While an overview of numerous clusters cannot be afforded here, one structure motivating for present study was a stable volleyball-shaped isomer [105]. One could speculate that its planar development, unfolding into a 2D-layer may turn rather stable as well. Direct computations confirmed indeed that this structure, dubbed B(1/8)-layer [106], has cohesive energy as good or even exceeding that of the established α-

sheet. More importantly, it posed a broader question of possible multiplicity of 2D-structures of comparable stability and if so, of their coexistence in two-dimensional formation. Since the layer serves as building block for fullerenes [70, 107], tubes [66, 108] and nanoribbons [3, 109, 110], understanding the B-layers intrinsic patterns and stability is a prerequisite for all those nanostructures [111].

B-layers are usually evaluated by density-functional theory (DFT) calculations [71, 72, 102] for specific structures derived from a close-packed triangular B sheet (denoted $B_{\triangle}$ hereafter) by selective removal of B atoms--a procedure that results in hexagonal voids, or "vacancies" (V). This leads to a very large number of possible configurations, exploring which poses a daunting combinatorial problem and hampers the direct use of first-principles methods. Hence, only a handful of B-layers have been considered so far.

5.2 Method: Cluster Expansion and DFT

Here we advance an approach to the structural diversity and stability of B-sheets based on the cluster expansion (CE) method [112] applied to the pseudo-alloy system $B_{1-x}V_x$ [113]. Vacancies in alloys can be treated routinely with the CE [114, 115] and here we demonstrate that CE provides a route to systematic first-principles study of B sheets.

In order to map the problem of the B-layers onto that of $B_{1-x}V_x$ pseudo-alloy structure, we consider the full $B_{\triangle}$ as being composed of a honeycomb or kagome [116] sublattice (B_V) and a triangular sublattice defined by the hexagon centers (Fig. 5.1, inset). The B_V sublattice is configurationally inactive, while each site of the triangular sublattice can be either a B atom or a vacancy V. The vacancy concentration is defined as $x = m/N$, where $m \in [0, n]$ $(n < N)$ is the number of V in a supercell of N lattice

sites of $B_{\triangle}$ [102, 117, 118]. To render various vacancy patterns, the rhombic 3×3, $\sqrt{12}\times\sqrt{12}$, and rectangular $4\times\sqrt{3}$ supercells can be initially employed, Fig. 5.1.

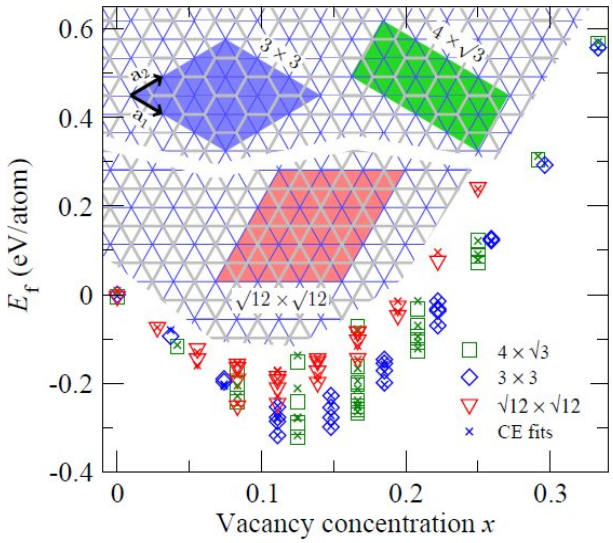

Figure 5.1 Formation energies E_f, according to Eq. (5.3.1), along with the corresponding CE fits as a function of vacancy concentration x in $B_{1-x}V_x$. Used supercells are shown in the inset. The arrows indicate the lattice basis vectors; the fixed, configurationally inactive B_V sublattice is shown in gray.

Then the stability of various B-layers can be assessed in terms of their formation energy E_f. Any lattice configuration can be described by a vector $\boldsymbol{\sigma} = (\sigma_1, \sigma_2, \ldots, \sigma_n)$, with $\sigma_i = +1$ where B atom is present or -1 if not (V). Within the CE formalism E_f for a configuration $\boldsymbol{\sigma}$ can be expressed as series [112, 119, 120]

$$E_f(\sigma) = J_0 + \sum_\alpha d_\alpha J_\alpha \overline{\Pi}_\alpha(\sigma) \qquad (5.2.1)$$

where d_α is the number of clusters of type α (e.g., pairs, triplets, etc.), J_α the corresponding effective cluster interaction, and $\overline{\Pi}_\alpha(\sigma) = \langle \Pi_i \sigma_i \rangle$ are the "spin" products for configuration $\boldsymbol{\sigma}$ averaged over all symmetry-equivalent α-type clusters. The ATAT (Alloy Theoretical Automated Toolkit [121]) is used to determine the expansion coefficients J_α by fitting the energies to their direct DFT-computed values, for a all

generated structures.

All DFT calculations were performed with the Quantum Espresso package [122], using ultrasoft pseudopotential in conjunction with the generalized gradient approximation to the electron exchange and correlation [40], employing plane-wave basis set with 30 Ry kinetic energy cutoff. All B-layer geometries were represented by supercells (insets in Fig. 5.1 and Fig. 5.3) with ≅ 10 Å vacuum region in normal direction. Summation over the Brillouin zone is carried out with a Monkhorst–Pack **k**-point set, ensuring approximately the same **k**-point density among different-size supercells, using as a reference 4×4×1 sampling for the 3×3 supercell, Fig. 5.1. All structures were fully relaxed until the force on each atom (E_{tot} change in the self-consistency loop) is less than 10^{-3} Ry/Bohr (10^{-4} Ry).

5.3 Results: Structure and Energy

For a supercell representing $B_{1-x}V_x$ at given x, the formation energy is calculated from the total energy *per atom* of the supercell, $E_{\text{tot}}(x)$, relative to that of the parent $B_{\triangle}$,

$$E_f(x) = E_{tot}(x) - E_{tot}(B_\Delta) \qquad (5.3.1)$$

Fig. 5.1 summarizes the DFT calculated $E_f(x)$ and the CE fits; relevant supercell parameters are collected in the Table 4.

supercell	N	n	C_{sym}	C_{DFT}	S_{CV}
4×√3	24	8	30	30	13.7
3×3	27	9	24	24	24.7
√12×√12	36	9	24	24	24.9
4×4	48	16	528	46	7.2
5×√3	30	10	78	31	6.3

Table 4 Various parameters of all supercells considered in the present work: N – total number of sites; n – number of configurationally active sites; C_{sym} – total number of symmetry inequivalent configurations; C_{DFT} – number of structures calculated with DFT; S_{CV} – cross validation score (meV/atom) of the best CE fit.

Note that the 2^n possible $\boldsymbol{\sigma}$-configurations are reduced by symmetries to reasonably small sets of $C_{sym} \leq 30$, and therefore one can exhaust all possibilities at the DFT level. As a standard measure of the CE quality we use the cross validation (CV) score [121], defined as

$$S_{CV} = (1/M)\sum_i \left(E_i^{DFT} - E_{(i)}^{CE} \right)^2 \qquad (5.3.2)$$

where $E_{(i)}^{CE}$ is fitted to the DFT calculated formation energies of M-1 other structures, excluding E_i^{DFT}. We have found that inclusion of up to five-point clusters is necessary to obtain good-quality fits, Table 4. As an illustration, Fig. 5.2 shows the clusters geometries for the 3×3 supercell along with the magnitudes of corresponding interactions. The dominant positive J's reflect the pairwise vacancy repulsion, whereas all nonvanishing three-point terms are attractive.

Not only Fig. 5.1 shows agreement between the CE- and DFT-computed energies and testifies to the power of CE method, but it also reveals the overall trend with expressed minimum around x ~ 0.1–0.15, where several most stable $B_{1-x}V_x$ structures are found (nearly degenerate in energy, within the computational accuracy). One is then compelled to explore this structural variability with the denser sampling which can be achieved by enlarging the supercells, as follows.

First we note that in the range of interest and higher x, the √12×√12 supercell based on the kagome lattice was the least efficient in detecting low energy structures and can be omitted. In this case, any pair of nearest-neighbor vacancies results in unfavorable four-fold bonding configuration of the shared B atom. Based on this observation, one can focus only on structures with configurationally inactive honeycomb sublattice.

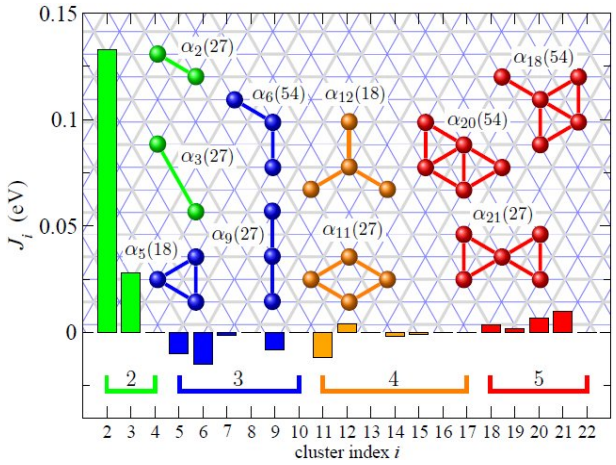

Figure 5.2 Effective cluster interactions J_i (excluding the empty and point clusters, i = 0, 1) for the 3×3 supercell (cf. Fig. 5.1), fitted with ATAT [121]. The clusters α_i ("figures") corresponding to the ten strongest interactions are shown as ball-and-stick models and the underlying grid represents the $B_\triangle$ lattice. Corresponding cluster multiplicities d_i, Eq. (5.2.1), are given in parentheses. The horizontal brackets group J's that correspond to the same cluster size k = 2−5.

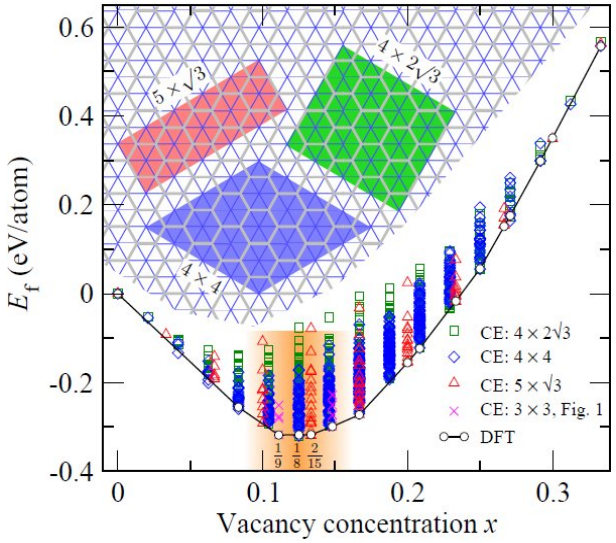

Figure 5.3 Formation energies E_f of all ≅ 2100 symmetry inequivalent structures calculated from CE fits to ≅ 130 configurations calculated with DFT, for the three supercells in the inset. Ground state checking is carried out with ATAT [121] only over the range $0.1 \leq x \leq 0.15$ (shaded region). For completeness, the values for the 3×3 supercell (Fig. 5.1) in this range of x, are also included. The exact fractions x that form a flat section of the DFT ground state line are indicated as well.

Accordingly, as a next step we enlarge the 3×3 to 4×4, and the 4×√3 to 4×2√3 and 5×√3 supercells (Fig. 5.3 and Table 4). Ideally, one would like to get the energies of larger supercells from Eq. (5.2.1) using the *J*'s calculated from smaller ones. In practice, we found the S_{CV} to be rather high and could not be improved any further because of the limited number of structures available for smaller supercells. We thus extended the DFT calculations to $C_{DFT} \cong 130$ selected structures, and the automated CE procedure [121] was run until very good CV scores were reached. The constructed CE's of Eq. (5.2.1) are then used to calculate the formation energies of *all* enumerated symmetry-nonequivalent configurations for these supercells and the results are shown in Fig. 5.3. This graph also reveals in greater detail the structural diversity of the stable B layers which, in fact, could already be anticipated from Fig. 5.1. The CE is fully consistent with the DFT "ground-state line" (as obtained with ATAT) practically over the entire range of *x* although ground state checking was explicitly requested only over the range indicated in Fig. 5.3. The most stable configurations have m=3–4 vacancies per 5×√3 and 3×3 supercells, and m=5–7 for the 4×4 and 4×2√3 supercells, which corresponds to the range $x \cong 0.1 - 0.15$ in $B_{1-x}V_x$. Distinguishing feature of the majority of these configurations is the presence of V clusters. Remarkably, we uncover a finite range $1/9 \le x \le 2/15$ where the DFT ground state line is flat, $E_f^{DFT}(x) = \text{const}$. At $x = 1/9$ it is straightforward to single out the most stable structure, the familiar α-sheet [70, 102], (Fig. 5.4a) as this V fraction is captured only by the relatively small 3×3 supercell, Fig. 5.1. At the two slightly higher vacancy fractions, $x = 1/8$ and $2/15$ are considerable number of geometries whose formation energies are within a few meV/atom of the

ground state line. The corresponding lowest-energy geometries are given in Fig. 5.4b-c, respectively.

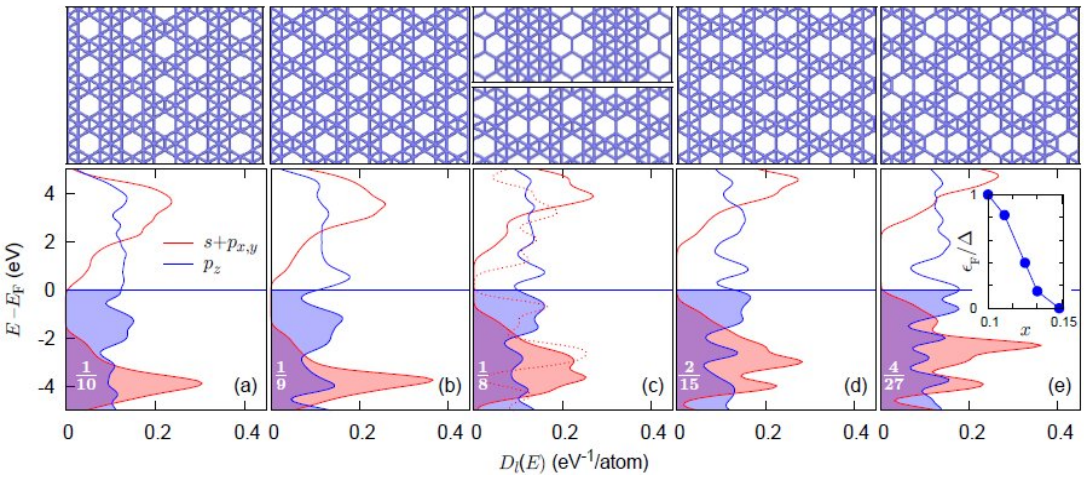

Figure 5.4 Projected density of states $D_l(E)$ (calculated using finer k-mesh and 0.3 eV Gaussian broadening) for some of the most stable B layers in the range $x \cong 0.1-0.15$ (exact x is indicated in the lower left corner). The corresponding patterns are shown above each. (b) shows the familiar α-sheet [102]; (c) the ground-state structure for $x = 1/8$ is shown in the lower segment of the image. The dashed line is $D_{s+px,y}(E) \equiv \Sigma_{l=s,px,py} D_l(E)$ of the highest energy structure (upper image segment) at the same x obtained using the $4\times\sqrt{3}$ supercell, Fig. 5.1. The inset in (e) shows the relative position of the scaled Fermi level $0 \le \varepsilon_F \le \Delta$ within the gap $\Delta(x)$ in $D_{s+px,y}(E)$ for the five structures.

It is evident from Fig. 5.3 that any fraction x outside the 0.1–0.15 range results in less favorable configurations, with substantially increasing E_f. Here we focus only on *flat* geometries. although out-of-plane atomic relaxation can have stabilizing effect [102, 118, 123]. However, such a buckling is shown to be important/operative only for denser layers, at $x < 1/9$ [118]. For the limiting case of $B_{\triangle}$, we calculated that buckling indeed reduced $E_f(0)$ by 0.15 eV/atom. This suggests that accounting for layer buckling can lead to less steep $E_f(x)$ line at $x \le 1/9$ but will not affect the most stable ordered configurations.

5.4 Results: Electronic Structure

To rationalize the $B_{1-x}V_x$ stability we analyze the electronic spectrum, viz. the projected density of states $D_l(E)$, of the found best structures in the range 0–0.15, Fig. 5.4. Clearly, all these structures are characterized by metallic p_z-derived band, with the Fermi level E_F falling in the gap $\Delta = \Delta(x)$ of the in-plane derived density of states $D_{s+px,y}(E)$. For clarity, the relative Fermi level position $\varepsilon_F \equiv E_F - E_0$ within the gap Δ, E_0 being the top of the filled $D_{s+px,y}(E)$, is plotted versus x in the inset of Fig. 5.4e. This hallmark in the electronic spectrum has been shown [102] to explain the stability of previously studied few B layers. Fig. 5.4 thus supports this stabilizing mechanism as broadly applicable, including a broad found family of almost isoenergetic phases of 2D-boron. The geometries shown in Fig. 5.4c-d constitute new ground-state structures of the planar B sheet which are as stable as the α-sheet [102] but have higher x.

It is interesting to note that the V pattern in the lower image segment of Fig. 5.4c ensures an optimal *mixing* with the denser $B_{\triangle}$, placing E_F approximately in the middle of Δ. To illustrate this effect, in the same panel we also plot $D_{s+px,y}(E)$ (dotted line) of the highest-energy structure (upper image segment) at the same $x = 1/8$ calculated with DFT using the $4\times\sqrt{3}$ supercell, cf. Fig. 5.1. This *phase-separated* V-$\triangle$ configuration has considerably reduced Δ.

5.5 Conclusion

In summary, we have combined DFT calculations with the CE method to explore the diversity of planar boron layers considered as a $B_{1-x}V_x$ pseudo-alloy. As a result we discover a number of two-dimensional stable polymorphs of nearly identical cohesive

energies. Distinctly different in structure, they all lie in the rather narrow range of vacancy concentration of 10-15%. This possibility of multiple structures-phases is in striking contrast to the other 2D-materials: carbon displays well known graphene structure, with only once discussed possibility of metallic pentaheptite [124], similarly h-BN displays distinct honeycomb structure [125] and no other known planar phases. For boron layers the emerging picture is that if they ever synthesized (likely, by a CVD on catalytic substrate or thermal decomposition of borides similar to graphene formation from SiC [126]), it will probably form co-planar patches of several polymorphs and thus large degree of disorder. This contrast with actively studied graphene, nitrides and sulfides makes further investigation of 2D-boron particularly intriguing.

Chapter 6
Metallacarboranes: Towards Promising Hydrogen Storage MOF

6.1 Introduction

Hydrogen is considered as a promising renewable non-polluting alternative to fossil fuels [127]. The success of hydrogen-based fuel cell depends upon materials, which can store hydrogen efficiently and reversibly at ambient conditions. An extensive search for efficient hydrogen storage materials led to finding of several promising candidates including metal hydrides [128-130], graphitic sorption nanomaterials [131, 132] and metal organic frameworks (MOF) [133, 134]. Although promising, these individual storage materials suffer from one or other form of practical difficulties, e.g. too strong metal-H binding in metal hydrides often results into poor kinetics, whereas too weakly physisorbed H_2 in graphitic nanostructures and in MOFs requires storage at very low temperature. Between strong chemisorption and weak physisorption there exists Kubas [135] type of interaction–a "non-classical" form of binding of H_2 to metal with a binding energy of ~0.4 eV/H_2–which is ideal for the reversible storage at ambient conditions. A single metal atom can bind multiple H_2 molecules [135, 136] via Kubas interaction leading to high gravimetric and volumetric density.

The possibility of storing hydrogen via Kubas interaction has been explored extensively for the case of transition metal (TM) decorated graphitic nanostructures [137-142] (nanotubes, fullerenes and graphene). Depending upon the type of metal atom, such complexes [139, 141] can store hydrogen up to 8 wt%. TM-ethylene complexes are once shown to store as much hydrogen [140, 143] as 14 wt%. The idea has been

extended to lighter metal decorated carbon materials [144, 145] as well, where significant storage has been predicted. These materials are promising and, if experimentally realized, can easily meet the material based DOE targets [146] for 2015. The biggest hurdle on the way to success of such materials is the tendency of metal atoms to aggregate [147, 148]. It has been shown [148] that TM atoms cluster on the surface of graphitic nanostructures, which significantly reduces the storage wt%. In order to prevent the clustering of metal atoms, the doping of carbon nanostructures by boron has been proposed [139]. Due to stronger B-TM binding, boron acts as an anchor to the metal atom. The practical difficulty of doping carbon nanostructures with boron remains a challenge for successful synthesis of such materials. So far there are no experimental reports on well-separated transition metal atoms on the boron-doped carbon nanostructures.

The key to the success of hydrogen storage via Kubas interaction may lie in finding nanomaterials where the metal atoms are among the constituent elements (and thus cannot aggregate), yet retain their H-binding ability. One such class is metallacarboranes [149], derived from the carboranes, one of the most studied classes of boron clusters. Carboranes are essentially borane clusters containing one or more carbon atoms. Replacing one or more BH units of carboranes by metal atoms leads to formation of metallacarboranes. The advantage of having both metal and C in the same cage has been utilized in various applications, including even nano-motors [150].

This sets the stage for investigation of hydrogen storage capacity of metallacarborane based MOF, further motivated by recent Farha *et al.* demonstration that icosahedral carborane based MOF can store up to 2 wt% of H_2 at 77 K via

physisorption [151, 152]. Here [153] we show that metal in metallacarboranes can bind multiple hydrogen molecules, while carbon can link the clusters to form three-dimensional frameworks. Replacing carboranes in MOF by metallacarboranes enhances the wt% due to adsorption of additional H_2 on metal atoms via Kubas interaction. This leads to storage of up to 8.8 wt% in metallacarbornes. Moving from a pure physisorption to Kubas type of H_2 binding increases the binding strength, which can ensure room temperature storage. The binding energies lie within the reversible adsorption range at ambient conditions. Sc and Ti are recognized as the most optimal metals in maximizing the storage capacity.

The calculations are performed using the density-functional theory based pseudopotential plane wave method as implemented in VASP [154, 155]. The ion-electron interaction is treated with all-electron projector-augmented wave (PAW) pseudopotentials [156, 157] using spin-polarized generalized gradient approximation of the Perdew–Burke–Ernzerhof (PBE) [158] for exchange and correlation. Gamma point is used for Brillouin zone sampling. Symmetry-unrestricted optimizations of both geometry and spin are performed using conjugate gradient scheme until the forces on every atom are less than 0.005 eV/Å. Large vacuum spaces (~15 Å) are used in supercells to minimize any cell-cell spurious interactions. Binding energy of the adsorbed hydrogen is defined as $E_b = (E(H_2)+E(\text{Adsorbent-}H_{m-2})-E(\text{Adsorbent-}H_m))/2$.

6.2 Hydrogen Storage

Aim of our study is to assess the hydrogen storage capacity of metallacarboranes and also to find out the best metal atom, which can maximize the number of adsorbed H_2 molecules. Due to computational limitations, the smallest metallacarborane $C_2B_4H_6M$,

(where M=Sc, Ti, V, Cr, Mn, Fe, Co, and Ni) is chosen to carry out the search for the optimal metal atoms. The optimized structure of $C_2B_4H_6M$ (MCB1) is shown in Fig. 6.1a. The ground state structures are spin polarized and magnetic moments change with the type of metal atoms, as shown in Table 5. The transition metal atoms keep their atomic magnetic moments, due to strong exchange splitting in spin-up and down states.

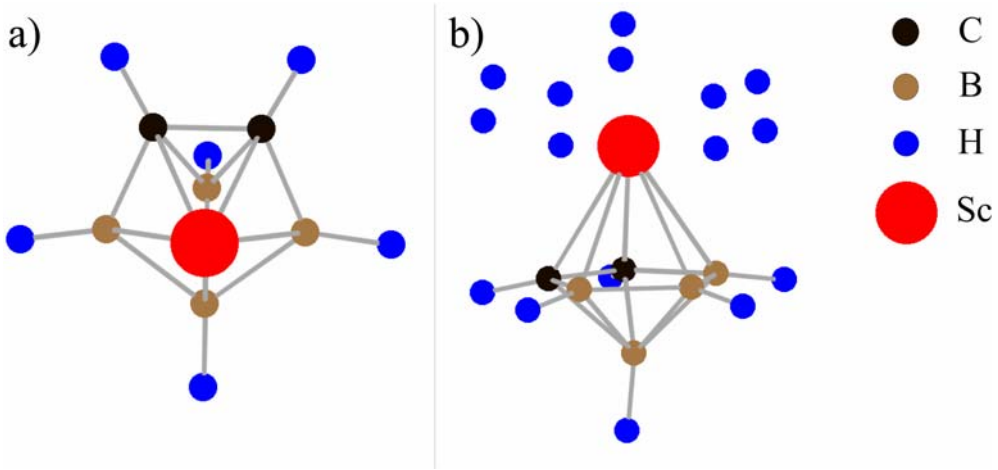

Figure 6.1 The optimized structures of (a) $C_2B_4H_6Sc$ (MCB1) and (b) fully hydrogen saturated $C_2B_4H_6Sc$-$5H_2$.

Hydrogen molecules are added subsequently to the MCB1, followed by unconstrained relaxation of the structure. As expected, the H_2 molecules bind to the metal via Kubas interaction [135], which is based on Lewis concept of donation of electron pairs. In such complex a σ-bonding electron pair (H:H) of H_2 molecule interact with the *d*-orbital of a metal via electron donation, Fig. 6.2. The uniqueness in the stabilization of M-H_2 complex is backdonation (BD), i.e., the retrodative donation of electrons from a filled metal *d*-orbital to the σ^* orbital of H-H bond. The BD is an important process in adding the H_2 to metal, in orienting the H_2 side-on to the metal, and in activating the dissociation of H-H bond. If the backdonation becomes too strong, it

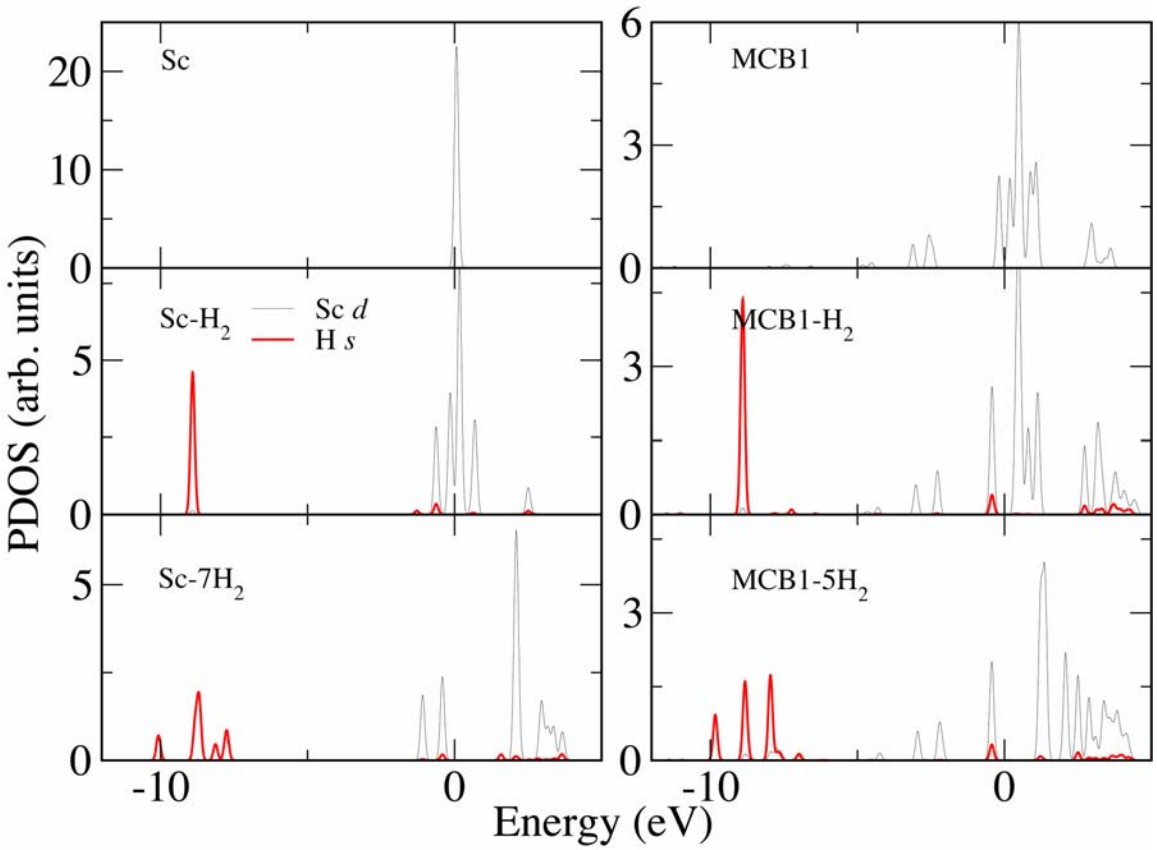

Figure 6.2 Orbital projected density of states (DOS) for different number of adsorbed hydrogen molecules on Sc (left column) and $C_2B_4H_6Sc$ (MCB1, right column). The black and red lines correspond to *d*- and *s*-orbitals of Sc and H, respectively. For clarity purposes the H-*s* DOS is enhanced by a factor of three. After the adsorption of first hydrogen molecule, there remain empty *d*-orbitals (peaks right after the Fermi level), which do not interact with H *s*-orbital. However, for the fully saturated Sc atom or MCB1 there are no such peaks available.

Leads to over-population of σ^* orbital and results into breaking of H-H bond and eventually leads to a strong M-H bonding as in metal hydride. On the other hand, a balance of BD and σ donation stabilizes the Kubas complexes. Generally, the H-H bond length, d_{HH}, is stretched about 15~25% over its value in free H_2 (0.74 Å). The d_{HH} is controlled by the ability of metal to backdonate electrons; therefore, varies with the change of metal atoms, Table 5.

The subsequent hydrogenation of MCB1 corresponding to each metal atom, is continued till cluster stops to bind any more H_2 molecules (Fig. 6.1b). Different metal atoms adsorb different number of hydrogen molecules. The H_2 storage capacity of a transition metal atom decreases with increasing number of *d*-electrons, Table 5. As the number of *d*-electrons increases, the ability of the metal atom to accept the σ donated electrons from H_2 decreases, which reduces the number of adsorbed H_2 molecules. Among the first row transition metal atoms, Sc and Ti have maximum number of available empty *d*-orbitals, therefore they adsorb largest number of H_2 molecules as shown in Table 5.

To evaluate the effect of cluster-cage on the binding ability of a TM, we analyze the hydrogen binding to Sc and Ti when they are in atomic form [135], as opposed to being part of metallacarborane. The hydrogen storage capacity of an isolated TM atom

M (# of *d*-electrons)	Magnetic Moment (μ_B)	Number of adsorbed H_2's	wt%	E_b (eV/H)	d_{HH} (Å)
Sc (1)	1	7	23.89	0.42-0.10	0.85-0.79
MCB1Sc (1)	1	5	7.85	0.26-0.10	0.84-0.78
MCB2Sc	1	5	5.38	0.26-0.01	0.79-0.77
MCB3Sc	2	10	8.81	0.21-0.01	0.79-0.77
MCB4Sc	0	8	6.38	0.17-0.08	0.81
Ti (2)	2	7	22.76	0.46-0.20	0.96-0.81
MCB1Ti (2)	2	5	7.68	0.38-0.13	0.85-0.77
MCB2Ti	2	5	5.29	0.34-0.12	0.84-0.77
MCB3Ti	4	8	6.93	0.32-0.16	0.78
MCB4Ti	2	6	4.75	0.25-0.03	0.80-0.78
MCB1V (3)	3	4	6.09	0.30-0.24	0.89-0.80
MCB1Cr (5)	4	3	4.60	0.38-0.25	0.90-0.80
MCB1Mn (5)	5	3	4.50	0.37-0.23	0.92-0.79
MCB1Fe (6)	4	3	4.47	0.56-0.04	0.92-0.83
MCB1Co (7)	3	3	4.38	0.58-0.05	0.92-0.76
MCB1Ni (8)	2	2	2.96	0.58-0.31	0.94-0.79

Table 5 The average magnetic moment, number of H_2s adsorbed, wt%, highest-lowest binding energies of H_2 and d_{HH} for different systems studied.

(Sc or Ti) is estimated. Since out of the two (Sc and Ti), Sc shows overall better hydrogen storage capacity (Table 5), we focus on Sc. The Sc atom adsorbs seven H_2 molecules before it saturates, two more than in the MCB1 cluster. Both steric and electronic effects cause the reduction in the number of adsorbed H_2 on MCB1. Geometrically, due to presence of carborane the H_2 molecule cannot bind to one side of the metal atom. Furthermore, the Sc atom interacts with the carborane via *d*-electrons following the donation-backdonation mechanism as shown in Fig. 6.2. This essentially reduces the available number of *d*-orbitals, which leads to adsorption of lesser number of hydrogen molecules on MCB1 as compared with the single metal atom. The overall binding behavior remains identical to the isolated atom. Fig. 6.2 shows the difference between the hybridization of the H_2 *s*- with the Sc *d*-orbitals upon the subsequent adsorption. In the case of Sc-H_2 there are still empty *d*-orbitals available to bind more H_2s, whereas after maximum adsorption every metal *d* peak has corresponding peak from H_2 *s*-orbitals. Same behavior can be seen for the Sc atom in the MCB1, Fig. 6.2. Overall, metal keeps most of its ability to adsorb hydrogen even in the MCB1. We should also note that the adsorbed hydrogen molecules in both cases (Sc and Ti) stay in associated form, with bond elongation within the range for Kubas type of binding (Table 5).

In a series of TM, the range of binding energies is given in Table 5. The E_b vary with the change of the metal atoms. Moving right in the periodic table, transition metal atoms tendency to donate *d*-electrons to the σ^* orbital increases, which leads to increased H-H bond length and stronger average binding energies, Table 5. The lesser number of

adsorbed hydrogen, increased binding energy, and weight of the late TM atoms eventually makes them less optimal for room temperature storage. Although Ti, V and Cr have optimal binding energies, due to lesser number of adsorbed H_2 molecules on V and Cr they will not be considered for further study. Sc and Ti based metallacarboranes store ~7.8 wt%, which is maximum among the first row TM atoms and will be considered for the evaluation of hydrogen storage capacity of larger clusters.

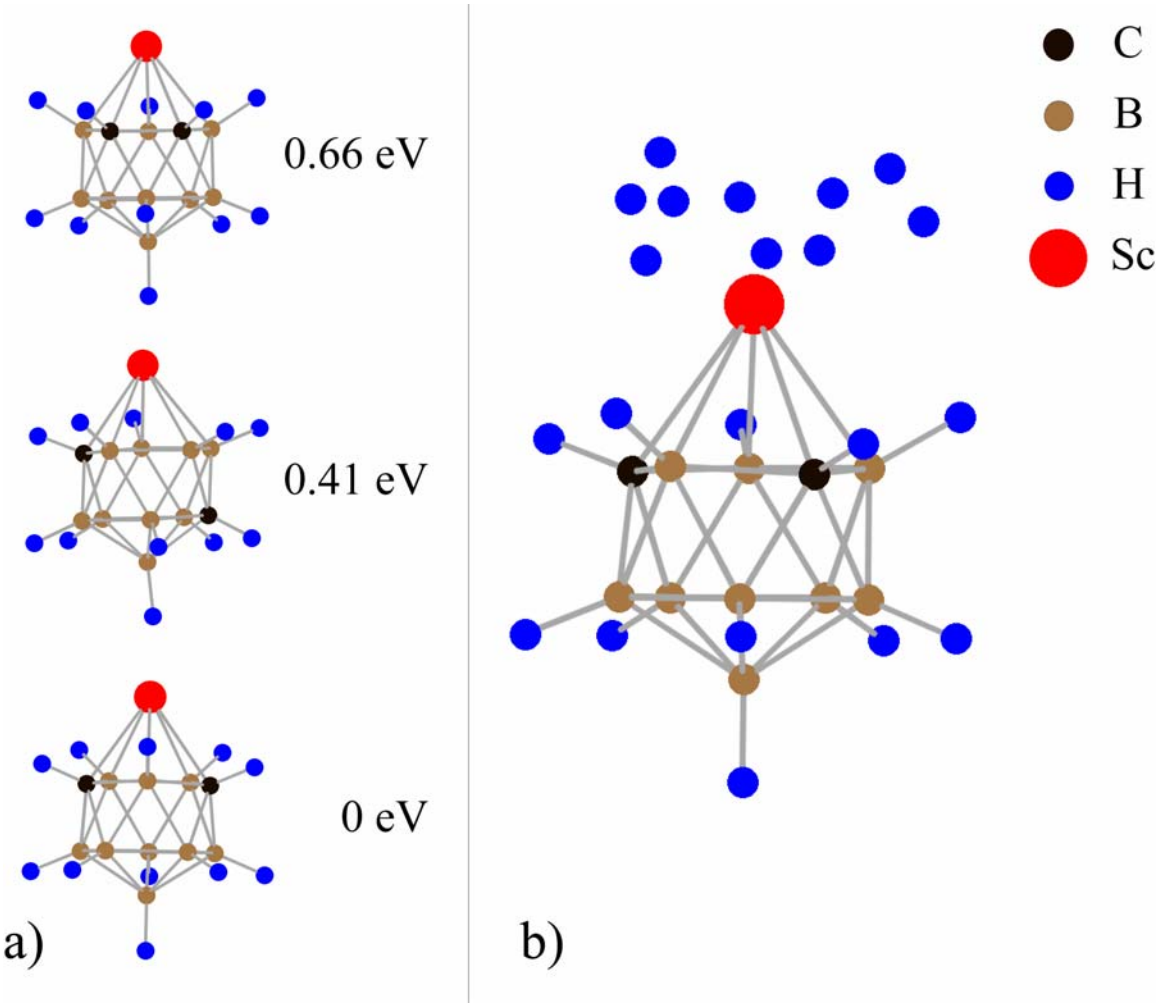

Figure 6.3 (a) The optimized structure of 1-2, 1-5, and 1-3-$C_2B_9H_{11}Sc$ (MCB2). The relative energies with respect to MCB2 are given. (b) The optimized structure of fully hydrogenated MCB2.

Next we estimated hydrogen storage capacities of more common metallacarborane clusters [149]. First, we consider $C_2B_9H_{11}M$ (M=Ti and Sc), derived from an icosahedral carborane. We calculated the binding energy of metal in three known isomers of $C_2B_{10}H_{12}$, by replacing one BH by a metal. Among the three non-equivalent positions of C atoms shown in Fig. 6.3, 1-3-$C_2B_9H_{11}M$ (MCB2) has the lowest energy. The two carbon atoms do not choose to stay adjacent to each other and prefer to be on a pentagonal ring, which is connected to the metal atom.

Upon subsequent hydrogenation of MCB2, both Sc and Ti adsorb five H_2 molecules via Kubas interaction. The H_2 wt% in this cluster is 5.38 and 5.30 % for Sc and Ti, respectively. The d_{HH} and E_b reduces slightly from the pentagonal-MCB1 case. This is not surprising, as it has been shown [135] that depending upon the ability to draw charge from the metal atoms, carborane cage influences the H_2 binding to the metal atom.

The storage capacity can be further enhanced if there is more than one metal atom in the metallacarborane cluster. In fact, most of the commonly observed metallacarboranes have two metal atoms. We study the $C_2B_8H_{10}M_2$ (M=Sc and Ti), where the metal atoms are at the two opposite apexes of the icosahedron. The positions of C atoms are optimized and among the non-equivalent structures of parent carborane, 1-5-$C_2B_8H_{10}M_2$ (MCB3) was found to be lowest in energy. In this configuration, each metal atom is bonded to four borons and one carbon. 1-3- and 1-2-$C_2B_8H_{10}M_2$ are 0.008 and 0.56 eV higher in energy, respectively. Upon hydrogenation, Sc (shown in Figure 6.4a) and Ti atoms totally adsorb ten and eight H_2s, respectively. The resulting wt% is 8.81 and 6.93 for Sc and Ti, respectively. The d_{HH} remains similar to the MCB2.

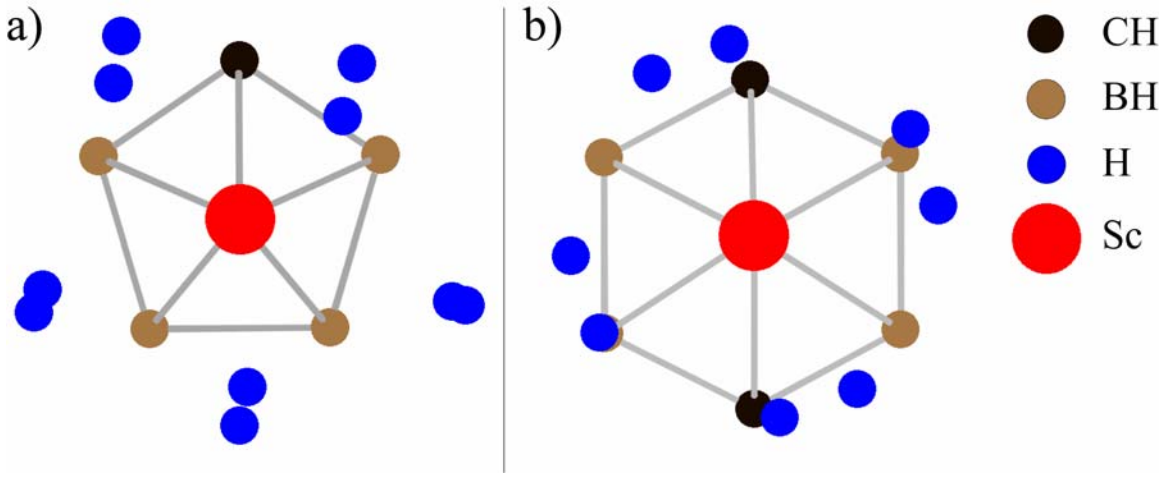

Figure 6.4 View along the Sc---Sc axis of the optimized fully hydrogenated structures of (a) pentagonal anti-prism 1-5-$C_2B_8H_{10}Sc_2$(MCB3)-10H_2 and (b) hexagonal anti-prism $C_4B_8H_{12}Sc_2$(MCB4)-8H_2.

Finally, we studied a slightly larger symmetric metallacarborane hexagonal anti-prism $C_4B_8H_{12}M_2$ (MCB4, M=Sc and Ti), having metal atoms at the two opposite apexes. Similar to previous cases, the hydrogen binds to metal atom via Kubas interaction. The Sc and Ti atoms adsorb eight and six H_2 molecules totally, resulting into 6.38 and 4.75 wt%, respectively, as shown in Fig. 6.4b. The average binding energies and magnetic moments show similar trends as observed in previous cases. Therefore, MCB4 can also store hydrogen in significant wt %. However, due to increase in number of atoms and volume of the cage, the gravimetric as well as volumetric capacities will be reduced.

The importance of presence of carbon atoms in the metallacarboranes is that they can bind to linkers such as Metal-carboxylate, which will connect these clusters in a three dimensional framework as demonstrated for the carborane based MOF [151]. Therefore, it is important to estimate how carboxylate affects the overall storage capacity of the metallacarboranes. We tested this by adding COOZn to carbon atom and

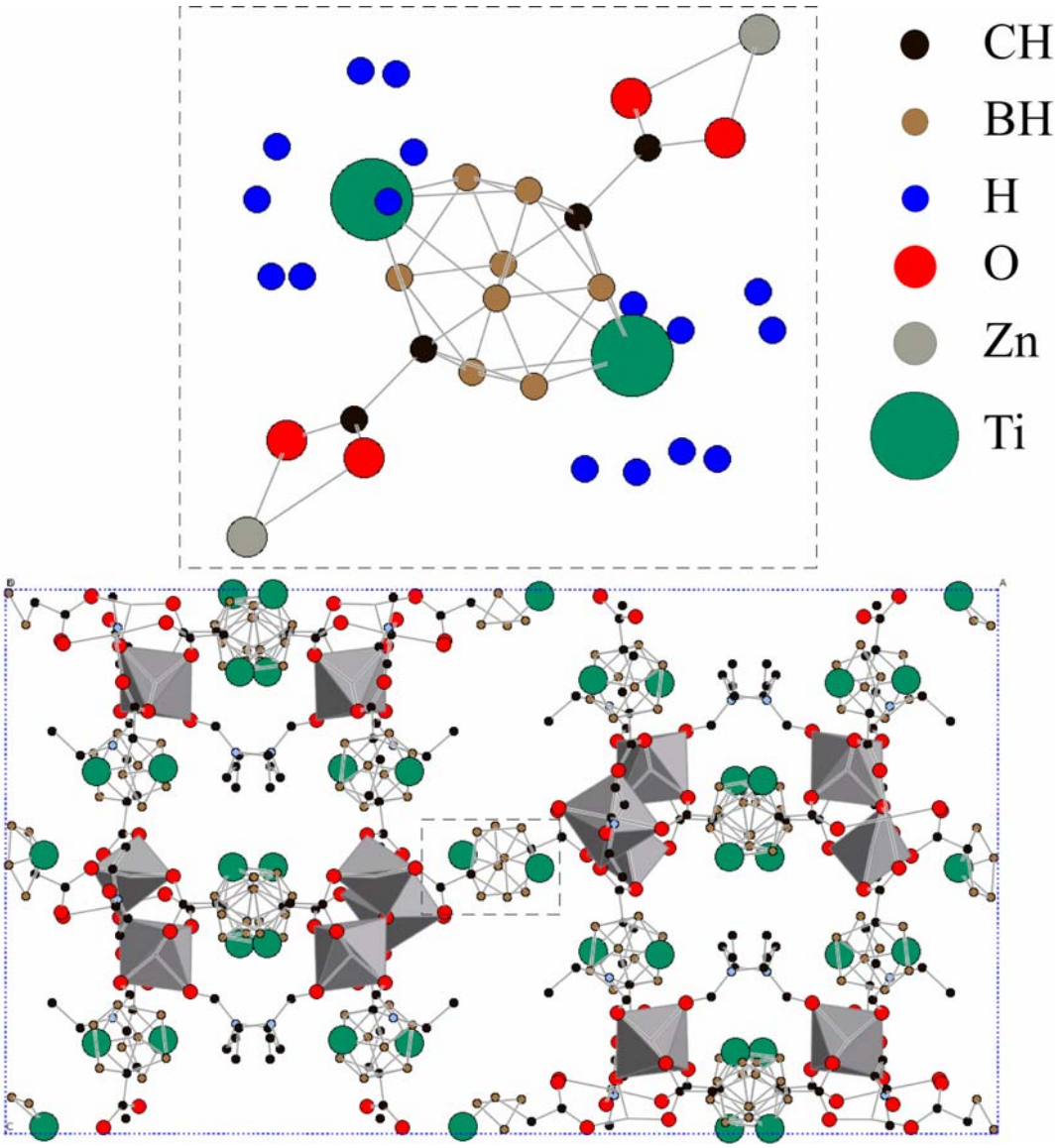

Figure 6.5 Optimized structure of corresponding 1-5-$C_2B_8H_{10}Ti_2$ (MCB3) with the Zn-carboxylate groups attached. Below shown is the likely structure of a MOF with MCB3 linkers, analogous to the experimentally reported [151] (here two BH units are replaced by Ti atoms in every carborane cage).

hydrogenated the cluster. The number of adsorbed H_2 molecules remains the same as in original metallacarborane. Each carboxylate group can attach up to four metallacarborane clusters. In the case of 1-5-$C_2B_8H_{10}Ti_2$ the wt% (calculated only considering Kubas type of H_2) reduces from 6.93 to 5.65 %, which is still larger than the DOE 2015 target [159]. Taking these into account we show a model structure of

Metallacarborane based MOF in Fig. 6.5. The structure is derived from the experimentally synthesized carborane MOF [151] by replacing two BH units by metal atoms. Such MOFs have larger pore size and could physisorb additional H_2 molecule, Fig. 6.5. This will further enhance the H_2 storage in the metallcarborane based MOFs. Therefore, metallacarborane based MOFs are indeed promising materials for efficient H_2 storage.

6.3 Conclusion

We show the viability of metallacarboranes as natural hydrogen storage materials. The metallacarboranes bind hydrogen via Kubas interaction, with the binding energies lying in the reversible storage range. The Sc and Ti are found to be the optimum metal atoms maximizing the number of stored H_2 molecules. Being an integral part of the metallacarboranes, Sc and Ti atoms do not cluster and remain isolated. Depending upon the structure, metallacarboranes can adsorb up to 8 wt% of hydrogen, which exceeds DOE goal for 2015 [159]. Furthermore, carboxylate based connectors have no effect on number of adsorbed H_2 molecules. Therefore, in addition to adsorbing H_2 via Kubas interaction, metallacarborane based MOFs will also physisorb H_2 in the pores. Given the recent progress made in the carborane based MOFs, and abundance of metallacarboranes, such materials can soon become experimental reality.

Chapter 7
Electron Transport of Nanotube-based Gas Sensors – An *ab initio* Study

7.1 Introduction

The utilization of semi-conducting single-walled carbon nanotubes (S-SWNT) as electro-chemical sensors has attracted much attention in the past few years, perhaps because it is one of the closest applications of nano-science to commercial arena [160]. It is particularly intriguing because detecting molecules at such low concentrations (~1 ppb) had not been achieved previously by other electrical sensors [161]. Following Kong et al.'s original report on detecting the gaseous molecules NO_2 and NH_3 [162], several experiments have been performed, mostly reconfirming the effect [161, 163, 164]. There have been some theoretical investigations as well, on the mechanism of adsorption and binding energies of such molecules on SWNTs [165-169]. However, a theoretical account for the effect of such adsorption on quantum conductance is still lacking.

This chapter is an attempt to fill the gap between the theory and experiment in explaining the observed change in electric conductance of a S-SWNT as a result of exposure to different concentrations of NO_2 gas molecules [170]. We calculate such conductance change for a (10,0) SWNT.

7.2 Results: Adsorption

The computations were based on Green's function formalism for conductance, in conjunction with density functional theory (DFT) calculation of electronic structures. For conductance calculations, TARABORD code [171] was used. DFT computations

were performed using Gaussian 03 package [51]. Generalized gradient corrected exchange and correlation functionals BLYP [42, 172] and 3-21G basis set were used for all electronic structure calculations. The initial relaxed structure for nanotube was obtained by Hartree-Fock (HF) approximation and 6-31G (d,p) basis set. The corresponding relaxed structure for NO_2 was obtained by MP2/6-31G (d, p).

There are several reports on the adsorption mechanism of NO_2 on SWNTs [165-169]. These results are mostly based on DFT calculation of the relaxed position of the molecule on the nanotube. The binding energies and the distances between the molecule and the nanotube, reported for adsorption on a (10,0) SWNT, are in the range of 0.3 to 0.8 eV and 2-3 Å, respectively [165-169], and correspond to physisorption. The results also show that within the same method, binding energies are not too sensitive to the orientation of the molecule or the position at which it is attached to the nanotube (difference in binding energies is of order of k_BT at room temperature). Noting this fact, we use one of the relaxed geometries with the lowest binding energy within LSDA approximation [169] for calculation of conductance. In this configuration, the nitrogen atom is located on top of a carbon atom and NO_2 molecule is parallel to the tangent plane to the nanotube, as shown in Fig. 7.1. Our calculations show that the main features in conductance change are the same for different orientations of the adsorbed molecules [173], therefore, the conclusions drawn later are applicable for those orientations as well. We consider three different surface-coverages (SCs), with a distance 2.7 Å between the nitrogen and the underlying carbon. It is useful to parameterize the SC by the number of NO_2 molecules per hexagon (θ). Therefore, the three cases in Fig. 7.1 correspond to θ =

2.5% (a), 5% (b) and 10% (c). Surface-coverage is obviously proportional to the gas concentration. The values used here for θ are chosen to lie in the range of experimental conditions, based on the relation [174]:

$$\theta = \frac{P}{\nu_0 \sqrt{2\pi m k_B T}} e^{E_B / k_B T} \qquad (7.2.1)$$

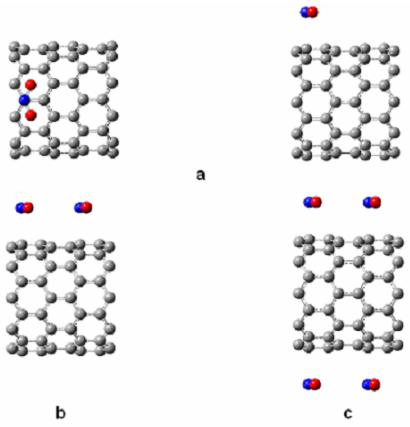

Figure 7.1 (a) Top (left) and side (right) views of the NO_2 molecule adsorbed on a (10,0) SWNT at the lowest surface-coverage (SC) with one molecule per two unit cells of the nanotube (θ = 2.5%). (b) Medium SC (one molecule per unit cell, θ = 5%). (c) High SC (two molecules per unit cell, θ = 10%).

where P is the pressure, ν_0 is the attempt frequency(10^{12} s^{-1}), m is the mass of the molecule (NO_2), T is the temperature and E_B is the binding energy. For $P = 5 \times 10^{-3}$ Pa and room temperature [169] we get θ = 0.1% (14.5%) for LSDA (LDA) value of the binding energy E_B = 0.5 eV (0.62 eV). It should be noted that Eq. (7.2.1) is valid when the adsorption sites are mostly free.

7.3 Results: Conductance

In order to calculate the conductance of the nanotube, we need the *ab initio* calculation of the Hamiltonian and overlap matrices (in atomic orbital basis) for the conducting channel and for each principal layer of the semi-infinite source and drain

contacts, as well as the corresponding coupling matrices between them [33, 171]. A principal layer consists of the minimum number of nanotube unit cells such that each layer interacts only with its nearest neighboring layers. The contacts here are periodic extensions of the conducting channel, i.e. S-SWNT with adsorbed NO_2 molecules. These matrices are needed to calculate the self-energies of the contacts ($\Sigma_{D,S}$), as well as the Green's function of the channel (G), which in turn will be used in Landauer-Buttiker formula for current (1.5.10).

Conductance as a function of carrier energies and bias voltage will be:

$$C(E,V) = \frac{2e^2}{h} T(E,V) \tag{7.2.2}$$

We calculate conductance at zero temperature and zero bias voltage. Correspondingly, in the actual case of lightly doped S-SWNT at low temperature and low bias (compared to the band gap) the area under the conductance curve from $E_f - eV/2$ to $E_f + eV/2$ gives the current by Eq. (1.5.10)(the Fermi-Dirac term will be zero outside this energy range).

Two unit cells of (10,0) SWNT are sufficiently large to be considered as a principal layer. Therefore, DFT computations were performed for a relatively large hydrogen-terminated nanotube (consisting of 7 unit cells), before and after NO_2 adsorption. Then, Hamiltonian and overlap matrix elements corresponding to the middle 4 unit cells (i.e. two principal layers) were extracted. The (identical) diagonal blocks were used as corresponding matrices for the conducting channel and each layer of the contacts. The off-diagonal blocks form the coupling matrices between the

channel and initial layer of each contact, as well as the coupling between adjacent layers in contacts [33, 171].

The density of states (DOS) and conductance plots for different concentrations of adsorbed NO_2 molecules are shown in Fig. 7.2. For pristine nanotube we observe a gap of 0.98 eV between the valence and conduction bands, which is in good agreement with well established reports (e.g. GGA result E_g = 0.88 eV [175]).

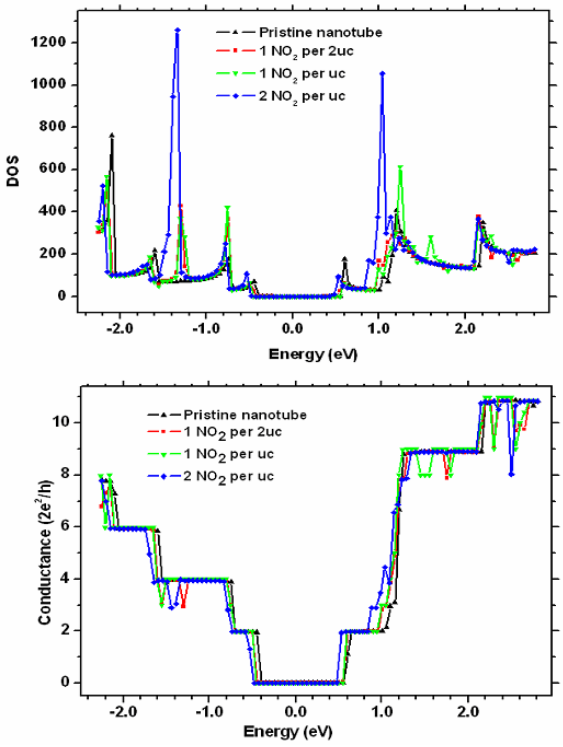

Figure 7.2 DOS (top) and conductance (bottom) as a function of energy of carriers, for different SCs.

Adsorption of NO_2 molecules results in additional van Hove singularities in DOS. One can easily identify two such peaks, which are common for all SCs: one around E = -1.4 eV and the other around E = 2.5 eV. Both of these peaks correspond to drop of conductance. To our understanding this is due to broken rotational symmetry around

the NT axis after NO_2 adsorption, which in turn results in widened inter-band spacing responsible for appearance of additional peaks and conductance drop.

The interesting feature here is the shift of conductance drops towards lower energies with increase of concentration. We can see the same effect in the conductance steps at usual van Hove singularities of S-SWNT. In Fig. 7.3 we show this shift with a higher resolution, around the bottom of conduction band. This shift in energy is due to the perturbation induced by the electric field of the NO_2 molecules on the nanotube, which can be estimated by average of electrostatic energy of carbon atoms in one unit cell of the nanotube in presence of NO_2 field (using Mulliken atomic charges).

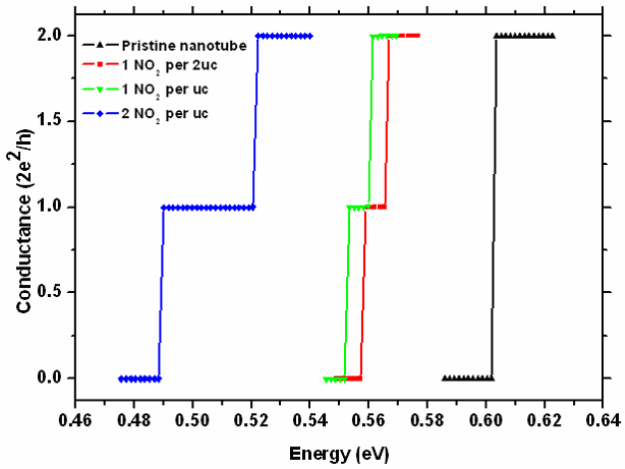

Figure 7.3 The shift in conductance towards lower energies at the minimum of conduction band. The shift increases with concentration.

Recalling that for small bias voltages, current is the area under the conductance curve within a small energy range around Fermi Energy, we expect a decrease (increase) of current for p-type (n-type) S-SWNTs with Fermi energies close to top (bottom) of the valence (conduction) band. Here by p-type or n-type, we refer to doping before NO_2 adsorption, which is due to substrate or functionalization of the

nanotube. From Fig. 7.3 we can also see that the device turn-off gate-voltage (negative for n-type and positive for p-type S-SWNTs) decreases (increases) for p (n)-doped nanotubes, as concentration increases.

The electron charge transfer from the tube to the molecule is small (~ 0.01 e, based on GGA calculations). Such charge transfer would lower the Fermi energy of the tube a few milli-electron volts, depending on the initial Fermi level of the tube before NO_2 adsorption (this estimate is based on the change of the area under DOS curve up to Fermi level, caused by a charge transfer of ~0.01 e). This change in Fermi level is very small. As a result, the effect of charge transfer, which would be the reverse of NO_2 dipole effect is negligible.

Both the current and the turn-off gate-voltage change explained above (based on the theory) are in odds with reported experimental results [161, 162, 164]. In experiments, the mechanism of NO_2 detection is far from obvious. In a recent paper, Zhang et al. propose that detection is due to changes at the interface between the nanotube and the electrodes, and not to the molecules adsorbed directly on the nanotube surface [176]. Earlier, Peng et al. suggest that the effect is not due to adsorption of NO_2, but rather NO_3 molecules, which are formed by chemical reactions between NO_2 molecules, allowed by low diffusion barrier between adsorption sites around the nanotube [169]. The reason for the above proposal is that the experimental value for recovery time at the room temperature (~12 h) is much larger than what the theory suggests (a few seconds, based on the calculated binding energies [169]).

In the original paper by Kong et al. [162], the authors offer a different explanation (other than direct adsorption on the nanotube surface) for the current change upon

exposure to NH_3 molecules. They attribute the effect to either binding of the gas molecules to hydroxyl groups on the SiO_2 substrate or interaction of NH_3 molecules and S-SWNT through other species (e.g. pre-adsorbed oxygen species on the nanotube). The reason for such an explanation was the belief that there was no affinity between NH_3 molecule and SWNT (this differs from some independent calculations results [165, 166]).

Given the ambiguity in the reason for the current change, we can see that a different scenario for NO_2 detection in reported experiments (other than adsorption on the tube) is quite possible. Indeed, as we show here, such direct adsorption would result in an opposite effect on current change in extrinsic S-SWNTs.

7.4 Conclusion

In conclusion, based on quantum conductance calculations, we show that for p-type (n-type) nanotubes with Fermi energies close to usual S-SWNT van Hove singularities, direct adsorption of NO_2 molecules should result in decrease (increase) of current under small drain-source biases. This is due to the shift of conductance curve to lower energies as a result of adsorption. This shift is more significant for higher concentrations. We argue that this effect is due to relatively strong electric dipole moments of the gas molecules, which induce localized electric dipoles on the tube and as a result lower the energy of the bands. We show that such a shift in energy decreases (increases) the turn-off gate-voltage of the device for p (n) type S-SWNTs. We must add that the fact that DFT methods usually underestimate band gaps does not change our conclusions since they are based on the shift of the bands and not absolute value of the gap. Also, all our calculations are spin polarized with energy difference of

less than 0.026 eV between spin-up and spin-down at the edge of valence and conduction bands. The plots are reported for spin-up values of energy, but since spin polarization effect is less than conductance steps shift (0.043 eV for lowest concentration), it doesn't change the conclusions (spin effect becomes less significant for higher concentrations).

Chapter 8
Electronic Properties of Twisted Armchair Graphene Nanoribbons

8.1 Introduction

Since the successful isolation of graphene sheets by mechanical exfoliation of pyrolytic graphite [177], there has been numerous studies on electronic and mechanical properties of graphene (for a review, see Ref. [178] for instance). Because of its very high charge carrier mobility [177, 179, 180], graphene has opened up great possibilities in electronic device applications.

Graphene nanoribbons (GNRs) are quasi one dimensional cuts of graphene. They can form zigzag, armchair or chiral edge patterns. Atoms along the edge of a zigzag GNR (ZGNR) come from the same sublattice of graphene, whereas atoms from two different sublattices form bonds along the edge of an armchair GNR (AGNR).

GNRs have been studied extensively [181-184]. Hydrogen terminated ZGNRs have ferromagnetic spin ordering along each edge and antiparallel spins for opposite edges [181]. There are different techniques for synthesizing GNRs; STM tip etching, [185] metallic nanoparticle atomically precise etching [186], and unzipping carbon nanotubes [187], to name a few.

It has been shown that all hydrogen terminated GNRs are semiconducting, with the band gap gradually going to zero for large widths [181]. Detailed electronic properties of GNRs vary with the edge pattern. AGNRs fall into three families, depending on their width. With N being the number of dimer lines in an AGNR, these families are N = 3p - 1, 3p, and 3p + 1, where “p” is a positive integer. According to Local Density

Approximation (LDA) calculations, the N = 3p - 1 family has narrow band gap [181]. The gap is inversely proportional to the width in all three families.

In this chapter [188], we present our results for the change in electronic structure caused by a twist in the ribbon [189]. We studied the N = 3p - 1 and N = 3p + 1 families of AGNRs, optimized their geometric configurations and calculated their band structure using DFT-based tight binding method [190] and helical symmetry [191, 192]. As will be shown later, in both families of ribbons, the band gap closes at some certain twist angle. This can be useful in some applications such as switches and sensors. For the N = 3p family the band gap doesn't close as a result of twist [193]. and for this reason it is not considered here. Also, ZGNRs are not considered since spin polarized calculations are needed for correct accounting of the ferromagnetic edge states, which are not included in our tight binding scheme. It should be mentioned that if the edges are not H-terminated, the twist will be spontaneous [194].

The use of helical symmetry is due to the fact that traditional unit cells for small twist angles become unlimitedly large and the computations become unfeasible.

8.2 Method

The program used is the Trocadero code [195] with helical symmetry implemented [196, 197]. The structures of flat hydrogen terminated GNRs are relaxed until the total energy reduction between steps is less than $3*10^{-5}$ eV. The unit cell sizes of the flat GNRs are varied until the size with lowest energy is found, to the precision of $3*10^{-4}$ eV. Twisted GNR structures are relaxed similarly, using the unit cell size of the flat GNRs in the case of unrelaxed unit cell, or optimized individually in the case of relaxed unit cell.

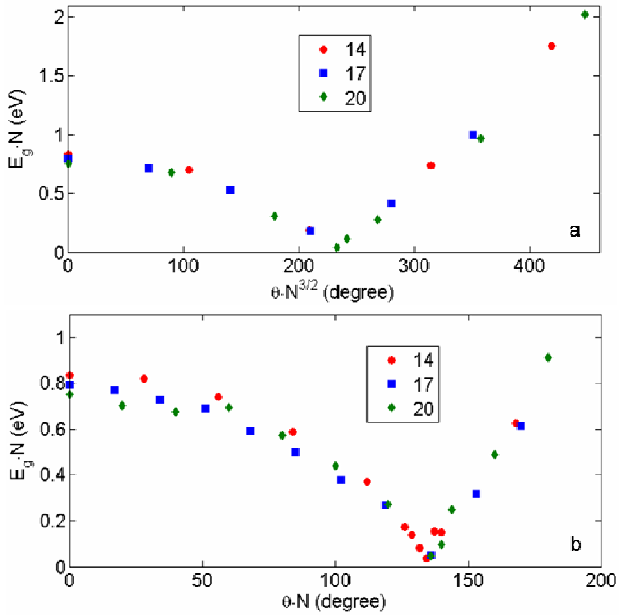

Figure 8.1 The scaled band gap as a function of scaled twist angle, for (a) unrelaxed unit cell size or (b) relaxed unit cell size, for N = 14, 17, 20 AGNRs.

8.3 Results: Electronic Structure and Energy

The N = 3p - 1 family is the narrow band gap case. It has been shown that the band gap closes with twist [193]. We consider relaxed and unrelaxed unit cell size for N = 14, 17 and 20 (Ref. [193] only considers the case where the unit cell size is fixed/unrelaxed). For unrelaxed unit cell size, the band gap closing angle (per unit cell) scales as $N^{-3/2}$. This is in agreement with Ref. [193] estimate. The band gap of the flat ribbon scales approximately as N^{-1}. Fig. 8.1(a) shows the scaled band gap E_g (eV) as a function of the scaled twist angle θ (degrees/unit cell) for all considered cases.

In the relaxed unit cell size case, the scaling is different. We obtained N^{-1} scaling for the band gap closing angle. Fig. 8.1(b) illustrates the behavior of the band gap as a function of the twist angle for all three widths considered.

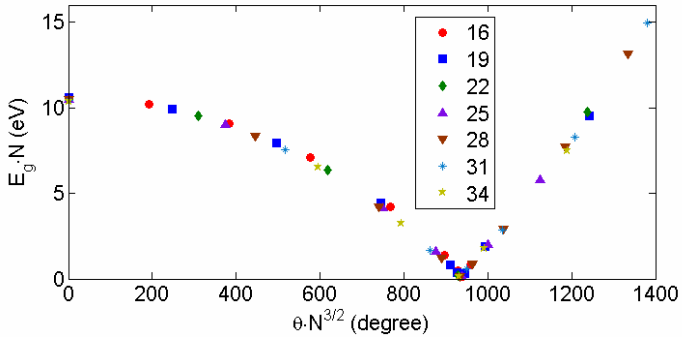

Figure 8.2 The scaled band gap as a function of scaled twist angle for unrelaxed unit cell size, for N = 16, 19, 22, 25, 28, 31, and 34 AGNRs.

For the N = 3p + 1 family also, the band gap closes with twist [193]. For this family of AGNRs, for unrelaxed case, we examined the band gap as a function of the twist angle for N = 16, 19, 22, 25, 28, 31, and 34. The scaling of $N^{-3/2}$ for the band gap closing angle and N^{-1} for the flat ribbon band gap applies here too. Fig. 8.2 shows the scaled band gap as a function of the scaled twist angle for all considered cases.

For this family of AGNRs, for the relaxed unit cell size case, the band gap decreases with twist but doesn't close at even large twist angles (more than 15 degrees/unit cell). At such large twist angles, the C-C bonds at the edge of the ribbon break. For this reason, we don't observe band gap closing.

Now, we turn our attention to energies of these structures. We calculated the strain energy per unit length (E_s/L where L is the relaxed or unrelaxed unit cell length) as a function of the twist angle per unit length (θ/L). Fig. 8.3 shows the plot. We obtain $E_s \sim \theta^{3.4}$ for N = 22. This is obviously out of the linear elastic regime, for which one expects $a \sim \theta^4$ relationship. Linear regime is defined by $(\theta/L)*w<<1$, where w is the width of GNR. In this case the linear regime criterion is violated (for the smallest twist angle we have $(\theta/L)*w = 0.32$).

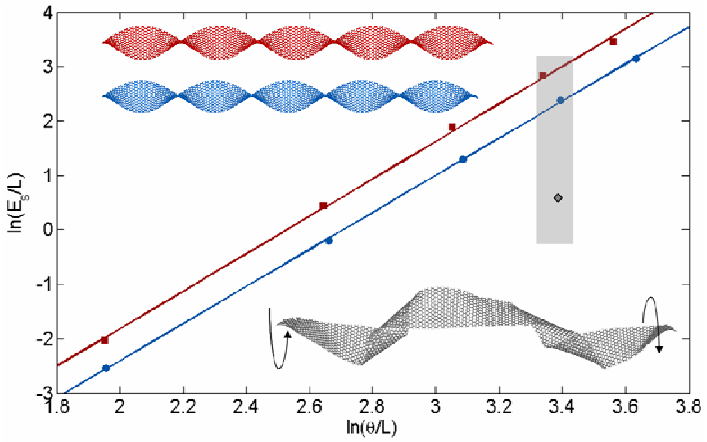

Figure 8.3 Logarithm of strain energy per unit length (E_s/L) as a function of logarithm of the twist angle per unit length (θ/L) for N = 22 AGNR. The red (blue) plot/ribbons correspond to unrelaxed (relaxed) unit cell size. The grey ribbon image shows the instability of the ribbon for relatively large twists (see text). The slopes of the curves give the $E_s \sim \theta^{3.4}$ power.

We also studied the band gap as a function of strain energy. It turns out that the band gap change is proportional to the strain energy. This is due to the fact that the bigger band gap change, the bigger change in the energy levels, and consequently, the total energy. It should be mentioned that the opposite is not necessarily true (we can have zero band gap that doesn't change with strain). Fig. 8.4 illustrates the results for N = 22 AGNR. The plot shows a close to linear relationship between the strain energy and band gap.

It should be mentioned that in the relaxed unit cell size case, at some certain twist angle, the ribbon may go off-axis. This is not the case when the unit cell size is fixed to the value for the flat ribbon, because the tension keeps the ribbon straight. Using helical symmetry, one can not detect such instability, since each unit cell is a replica of the previous unit cell with twist and translation along the axis. But since we are interested in the band structure of the twisted ribbons, we limit ourselves to helically symmetric

regime and don't consider such deformations. We note that for small twist angles, such instability doesn't occur, and the critical twist angle at which the ribbon bends off-axis is smaller for wider ribbons.

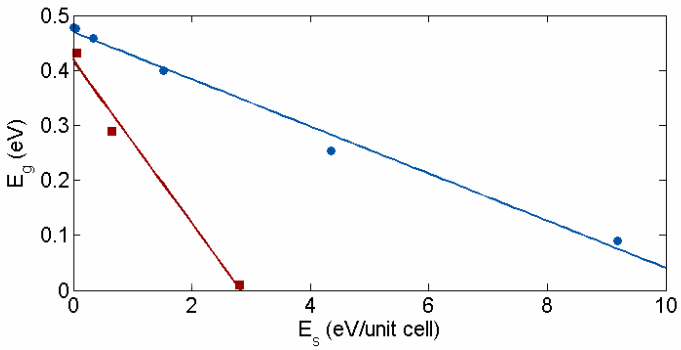

Figure 8.4 Band gap vs. strain energy for unrelaxed (red) and relaxed (blue) N = 22 AGNR.

8.4 Results: Conductance

Finally, we calculated conductance of flat and θ = 30 degrees/unit cell twisted N=7 AGNR around Fermi level, using nonequilibrium Green's function formulation [198]. The results for conductance and density of states (DOS) are shown in Fig. 8.5. As mentioned before, for the twisted ribbon, traditional unit cell can be quite large. Usually one uses the translational unit cell as building blocks for the principle layer for conductance calculations. A principle layer consists of the minimum number of unit cells so that each layer only interacts with the nearest neighboring layers. Applying helical symmetry, we choose the principle layer for conductance calculation to be much smaller than traditional unit cell (only 3 ribbon unit cells, where traditional unit cell for θ = 30 degree/unit cell consists of 12 ribbon cells, and can be unlimitedly large for small twist angles). We have verified that using this reduced unit cell as principle layer, we obtain the same results for conductance as using traditional unit cell. The critical point is

that the Hamiltonian and overlap matrices should be invariant under the symmetry transformation. This requires that the p orbitals (in a 4 orbital/carbon tight binding approximation) be rotated under a helical symmetry transformation. For this reason, this doesn't work in usual atomic based DFT basis, where the basis doesn't rotate under helical transformation.

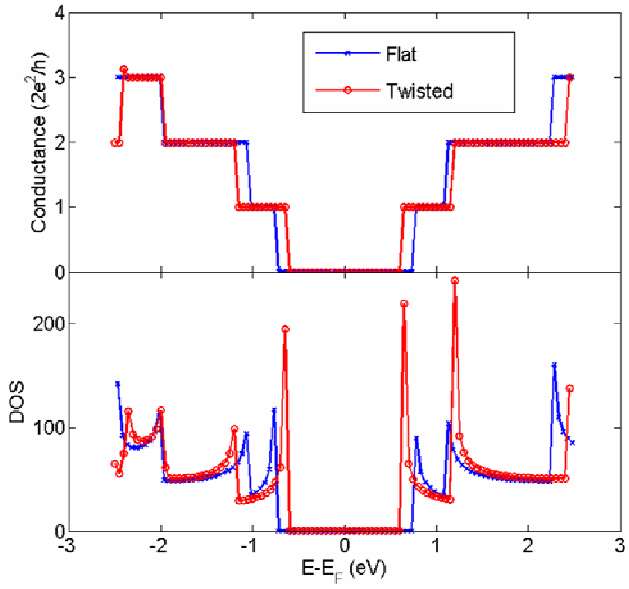

Figure 8.5 Conductance (top) and Density of States (bottom) of flat (blue) and twisted (red) ribbon around Fermi level. The steps in conductance plot correspond to van Hove singularities of DOS.

8.5 Conclusion

In conclusion, we studied the change in electronic structure of two families of AGNRs; N = 3p - 1 and N = 3p + 1, as a result of twist around the axis. The band gap closes at a certain twist angle which scales as $N^{-3/2}$ for unrelaxed and as N^{-1} for relaxed unit cell size. This can be useful for switches or sensors applications. We found a direct linear relationship between band gap and strain energy. We also investigated into the dependence of conductance and DOS on energy of carriers with or without twist. We

finally note that finite temperatures may lift the effects of spin polarization in ZGNR, rendering the tight binding approximation applicable, which reveals no band gap sensitivity to torsion.

References

[1] R. N. Grimes, J. Chem. Educ. **81**, 657 (2004).
[2] A. Quandt, and I. Boustani, ChemPhysChem **6**, 2001 (2005).
[3] T. T. Xu, J.-G. Zheng, N. Wu, A. W. Nicholls, J. R. Roth, D. A. Dikin, and R. S. Ruoff, Nano Lett. **4**, 963 (2004).
[4] B. Kiran, S. Bulusu, H.-J. Zhai, S. Yoo, X. C. Zeng, and L.-S. Wang, Proc. Natl. Acad. Sci. USA **102**, 961 (2005).
[5] D. Ciuparu, R. F. Klie, Y. Zhu, and L. Pfefferle, J. Phys. Chem. B **108**, 3967 (2004).
[6] B. F. Decker, and J. S. Kasper, Acta Crystallogr **12**, 503 (1959).
[7] B. Callmer, Acta Crystallogr., Sect. B: Struct. Crystallogr. Cryst. Chem **33**, 1951 (1977).
[8] A. W. Laubengayer, D. T. Hurd, A. E. Newkirk, and J. L. Hoard, J. Am. Chem. Soc. **65**, 1924 (1943).
[9] A. R. Oganov, J. Chen, C. Gatti, Y. Ma, Y. Ma, C. W. Glass, Z. Liu *et al.*, Nature **457**, 863 (2009).
[10] D. Li, Y.-N. Xu, and W. Y. Ching, Phys. Rev. B **45**, 5895 (1992).
[11] J. L. Hoard, D. B. Sullenger, C. H. L. Kennard, and R. E. Hughes, Journal of Solid State Chemistry **1**, 268 (1970).
[12] E. D. Jemmis, and D. L. V. K. Prasad, J. Solid State Chem. **179**, 2768 (2006).
[13] A. Masago, K. Shirai, and H. Katayama-Yoshida, Phys. Rev. B **73**, 104102 (2006).
[14] L. Hanley, and S. L. Anderson, J. Chem. Phys. **89**, 2848 (1988).
[15] L. Hanley, J. Whitten, and S. L. Anderson, J. Phys. Chem. **92**, 5803 (1988).
[16] S. J. La Placa, P. A. Roland, and J. J. Wynne, Chem. Phys. Lett. **190**, 163 (1992).
[17] I. Boustani, Phys. Rev. B **55**, 16426 (1997).
[18] I. Boustani, and A. Quandt, Europhys. Lett. **39**, 527 (1997).
[19] I. Boustani, A. Rubio, and J. Alonso, Chem. Phys. Lett. **311**, 21 (1999).
[20] S. Chacko, D. G. Kanhere, and I. Boustani, Phys. Rev. B **68**, 035414 (2003).
[21] H.-J. Zhai, B. Kiran, J. L. Li, and L.-S. Wang, Nat. Mater. **2**, 827 (2003).
[22] M. F. Hawthorne, Pure & Appl. Chem. **63**, 327334 (1991).
[23] Y. Zhao, M. T. Lusk, A. C. Dillon, M. J. Heben, and S. B. Zhang, Nano Lett. **8**, 157 (2008).
[24] M. F. Hawthorne, J. I. Zink, J. M. Skelton, M. J. Bayer, C. Liu, E. Livshits, R. Baer *et al.*, Science **303**, 1849 (2004).
[25] S. Iijima, Nature **354**, 56 (1991).
[26] J. Gavillet, Ph.D. thesis, ONERA–Universitè Paris VI (2001).
[27] D. S. Bethune, C. H. Kiang, M. S. d. Vries, G. Gorman, R. Savoy, J. Vazques, and R. Beyers, Nature (London) **363**, 605 (1993).
[28] S. Iijima, and T. Ichihashi, Nature (London) **361**, 603 (1993).
[29] T. Guo, C.-M. Jin, and R. E. Smalley, Chem. Phys. Lett. **243**, 49 (1995).
[30] J.-C. Charlier, X. Blase, and S. Roche, Rev. Mod. Phys. **79**, 677 (2007).

[31] R. Saito, G. Dresselhaus, and D. M. S, *Physical Properties of Carbon Nanotubes* (Imperial College, London, 1998), p. 259.
[32] M. Burghard, Surface Science Reports **58**, 1 (2005).
[33] M. P. Lopez Sancho, J. M. Lopez Sancho, and J. Rubio, J. Phys. F: Met. Phys. **14**, 1205 (1984).
[34] W. Tian, S. Datta, S. Hong, R. Reifenberger, J. I. Henderson, and C. P. Kubiak, J. Chem. Phys. **109**, 2874 (1998).
[35] M. B. Nardelli, Phys. Rev. B **60**, 7828 (1999).
[36] A. Rochefort, P. Avouris, F. Lesage, and D. R. Salahub, Phys. Rev. B **60**, 13824 (1999).
[37] P. Hohenberg, and W. Kohn, Phys. Rev. **136**, B864 (1964).
[38] J. P. Perdew, and A. Zunger, Phys. Rev. B **23**, 5048 (1981).
[39] J. P. Perdew, and Y. Wang, Phys. Rev. B **45**, 13244 (1992).
[40] J. P. Perdew, K. Burke, and M. Ernzerhof, Phys. Rev. Lett. **77**, 3865 (1996).
[41] A. D. Becke, Phys. Rev. A **38**, 3098 (1988).
[42] C. Lee, W. Yang, and R. G. Parr, Phys. Rev. B **37**, 785 (1988).
[43] A. D. Becke, J. Chem. Phys. **98**, 5648 (1993).
[44] D. E. H. Jones, New Scientist **35**, 245 (1966).
[45] E. Osawa, Kagaku **25**, 854 (1970).
[46] D. A. Bochvar, and E. G. Gal'pern, Proc. Acad. Sci. USSR **209**, 610 (1973).
[47] H. Kroto, J. Heath, S. O'Brien, R. Curl, and R. Smalley, Nature **318**, 162 (1985).
[48] N. G. Szwacki, A. Sadrzadeh, and B. I. Yakobson, Phys. Rev. Lett. **98**, 166804 (2007).
[49] S. Baroni, A. D. Corso, S. d. Gironcoli, P. Giannozzi, C. Cavazzoni, G. Ballabio, S. Scandolo *et al.*, http://www.pwscf.org/.
[50] D. Vanderbilt, Phys. Rev. B **41**, 7892 (1990).
[51] M. J. Frisch, G. W. Trucks, H. B. Schlegel, G. E. Scuseria, M. A. Robb, J. R. Cheeseman, J. J. A. Montgomery *et al.*, *Gaussian 03, revision B.03* (Gaussian, Inc., Wallingford, CT, 2004).
[52] P. C. Hariharan, and J. A. Pople, Theor. Chim. Acta **28**, 213 (1973).
[53] M. A. L. Marques, and S. Botti, J. Chem. Phys. **123**, 014310 (2005).
[54] T. Dumitrica, M. Hua, and B. I. Yakobson, Phys. Rev. B **70**, 241303 (2004).
[55] J. Nocedal, and S. J. Wright, *Numerical optimization* (Springer Verlag, New York, 1999).
[56] K. N. Kudin, G. E. Scuseria, and B. I. Yakobson, Phys. Rev. B **64**, 235406 (2001).
[57] P. Jena, and A. W. Castleman, Jr., Proc. Natl. Acad. Sci. USA **103**, 10560 (2006).
[58] I. Higashi, and K. Kobayashi, J. Solid State Chem. **133**, 16 (1997).
[59] S. Blair, D. Stentz, H. Feller, R. Leelasagar, C. Goater, S. Feller, and M. Affatigato, J. Non-Cryst. Solids **293-295**, 490 (2001).
[60] R. Debnath, and R. Sahoo, Curr. Sci. **87**, 975 (2004).
[61] N. G. Szwacki, A. Sadrzadeh, and B. I. Yakobson, Phys. Rev. Lett. **100**, 159901 (2008).
[62] G. Gopakumar, M. T. Nguyen, and A. Ceulemans, Chem. Phys. Lett. **450**, 175 (2008).

[63] M. S. Dresselhaus, G. Dresselhaus, and P. C. Eklund, *Science of Fullerenes and Carbon Nanotubes: Their Properties and Applications* (Academic Press, London, 1996).
[64] H. Tang, and S. Ismail-Beigi, Phys. Rev. Lett. **99**, 115501 (2007).
[65] X. Yang, Y. Ding, and J. Ni, Phys. Rev. B **77**, 041402 (2008).
[66] A. K. Singh, A. Sadrzadeh, and B. I. Yakobson, Nano Lett. **8**, 1314 (2008).
[67] L. A. Chernozatonskii, P. B. Sorokin, and B. I. Yakobson, JETP Letters **87**, 489 (2008).
[68] D. L. V. K. Prasad, and E. D. Jemmis, Phys. Rev. Lett. **100**, 165504 (2008).
[69] J. Zhao, L. Wang, F. Li, and Z. Chen, J. Phys. Chem. A **114**, 9969 (2010).
[70] A. Sadrzadeh, O. V. Pupysheva, A. K. Singh, and B. I. Yakobson, J. Phys. Chem. A **112**, 13679 (2008).
[71] J. Kunstmann, and A. Quandt, Phys. Rev. B **74**, 035413 (2006).
[72] K. C. Lau, and R. Pandey, J. Phys. Chem. C **111**, 2906 (2007).
[73] Z. Chen, and R. B. King, Chem. Rev. **105**, 3613 (2005).
[74] W. A. de Heer, Rev. Mod. Phys. **65**, 611 (1993).
[75] M. Buhl, and A. Hirsch, Chem. Rev. **101**, 1153 (2001).
[76] http://www.orbitals.com/orb/orbtable.htm.
[77] I. B. Bersuker, *Electronic Structure and Properties of Transition Metal Compounds: Introduction to the Theory* (Wiley, New York, 1996).
[78] K. C. Lau, R. Pati, R. Pandey, and A. C. Pineda, Chem. Phys. Lett **418**, 549 (2006).
[79] I. Cabria, M. J. Lopez, and J. A. Alonso, Nanotechnology **17**, 778 (2006).
[80] J. Miller, Physics Today **60**, 20 (2007).
[81] B. I. Yakobson, and R. E. Smalley, American Scientist **85**, 324 (1997).
[82] S. J. Tans, M. H. Devoret, H. J. Dai, A. Thess, R. E. Smalley, L. J. Geerligs, and C. Dekker, Nature **386**, 474 (1997).
[83] K. N. Kudin, G. E. Scuseria, and B. I. Yakobson, Phys. Rev. B **64**, 235406 (2001).
[84] E. Hernandez, C. Goze, P. Bernier, and A. Rubio, Phys. Rev. Lett. **80**, 4502 (1998).
[85] D. Sanchez-Portal, E. Artacho, J. M. Soler, A. Rubio, and P. Ordejon, Phys. Rev. B **59**, 12678 (1999).
[86] B. I. Yakobson, and P. Avouris, Topics Appl. Phys. **80**, 287 (2001).
[87] M. Terrones, J. M. Romo-Herrera, E. Cruz-Silva, F. Lpez-Uras, E. Muoz-Sandoval, J. J. Velsquez-Salazar, H. Terrones *et al.*, Materials Today **10**, 30 (2007).
[88] A. Loiseau, F. Willaime, N. Demoncy, G. Hug, and H. Pascard, Phys. Rev. Lett. **76**, 4737 (1996).
[89] J. P. Perdew, K. Burke, and M. Ernzerhof, Phys. Rev. Lett. **77**, 3865 (1996).
[90] G. Kresse, and J. Furthmüller, Comput. Mat. Sci. **6**, 15 (1996).
[91] G. Kresse, and J. Hafner, Phys. Rev. B **47**, 558 (1993).
[92] G. Kresse, and D. Joubert, Phys. Rev. B **59**, 1758 (1999).
[93] P. E. Blöchl, Phys. Rev. B **50**, 17953 (1994).
[94] L. D. Landau, and E. M. Lifshitz, *Elasticity Theory* (Pergamon, New York, 1986).
[95] B. I. Yakobson, and L. S. Couchman, J. Nanoparticle Research **8**, 105 (2006).

[96] S. Reich, C. Thomsen, and J. Maultzsch, *Carbon Nanotubes: Basic Concepts and Physical Properties* (Wiley, Berlin, 2004).
[97] P. Ball, nature materials **9**, 6 (2010).
[98] B. Kiran, S. Bulusu, H. J. Zhai, S. Yoo, X. C. Zeng, and L. S. Wang, Proc. Natl. Acad. Sci. USA **102**, 961 (2005).
[99] W. Huang, A. P. Sergeeva, H.-J. Zhai, B. B. Averkiev, L.-S. Wang, and A. I. Boldyrev, Nature Chemistry **2**, 202 (2010).
[100] E. Oger, N. R. M. Crawford, R. Kelting, P. Weis, M. M. Kappes, and R. Ahlrichs, Angew. Chem. Int. Ed. **46**, 8503 (2007).
[101] L. Pfefferle, and D. Ciuparu, edited by W. I. P. OrganizationUSA, 2005).
[102] H. Tang, and S. Ismail-Beigi, Phys. Rev. Lett. **99**, 115501 (2007).
[103] H. Li, N. Shao, B. Shang, L.-F. Yuan, J. Yang, and X. C. Zeng, Chem. Commun. **46**, 3878 (2010).
[104] D. L. V. K. Prasad, and E. D. Jemmis, Phys. Rev. Lett. **100**, 165504 (2008).
[105] X.-Q. Wang, Phys. Rev. B **82**, 153409 (2010).
[106] A. Sadrzadeh, H. Lee, and B. I. Yakobson, Unpublished.
[107] C. Ozdogan, S. Mukhopadhyay, W. Hayami, Z. B. Guvenc, R. Pandey, and I. Boustani, J. Phys. Chem. C **114**, 4362 (2010).
[108] V. Bezugly, J. Kunstmann, B. Grundkootter-Stock, T. Frauenheim, T. Niehaus, and G. Cuniberti, ACS Nano **5**, 4997 (2011).
[109] S. Saxena, and T. A. Tyson, Phys. Rev. Lett. **104**, 245502 (2010).
[110] Y. Ding, X. Yang, and J. Ni, Appl. Phys. Lett. **93**, 043107 (2008).
[111] S. Er, G. A. de Wijs, and G. Brocks, J. Phys. Chem. C **113**, 18962 (2009).
[112] J. M. Sanchez, F. Ducastelle, and D. Gratias, Physica A **128**, 334 (1984).
[113] E. S. Penev, S. Bhowmick, A. Sadrzadeh, and B. I. Yakobson, Nano Lett. **12**, 2441 (2012).
[114] G. L. W. Hart, and A. Zunger, Phys. Rev. Lett. **87**, 275508 (2001).
[115] A. Van der Ven, and G. Ceder, Phys. Rev. B **71**, 054102 (2005).
[116] M. Mekata, Phys. Today **56**, 12 (2003).
[117] H. Tang, and S. Ismail-Beigi, Phys. Rev. B **80**, 134113 (2009).
[118] H. Tang, and S. Ismail-Beigi, Phys. Rev. B **82**, 115412 (2010).
[119] S. Muller, J. Phys.: Cond. Matter **15**, R1429 (2003).
[120] A. V. Ruban, and I. A. Abrikosov, Rep. Prog. Phys. **71**, 046501 (2008).
[121] A. van de Walle, M. Asta, and G. Ceder, Calphad **26**, 539 (2002).
[122] P. Giannozzi, S. Baroni, N. Bonini, M. Calandra, R. Car, C. Cavazzoni, D. Ceresoli *et al.*, J. Phys.: Cond. Matter **21**, 395502 (2009).
[123] I. Cabria, J. A. Alonso, and M. J. Lopez, Phys. Stat. Sol. (a) **203**, 1105 (2006).
[124] V. H. Crespi, L. X. Benedict, M. L. Cohen, and S. G. Louie, Phys. Rev. B **53**, R13303 (1996).
[125] D. Golberg, Y. Bando, Y. Huang, T. Terao, M. Mitome, C. Tang, and C. Zhi, ACS Nano **4**, 2979 (2010).
[126] W. A. d. Heer, C. Berger, M. Ruan, M. Sprinkle, X. Li, Y. Hu, B. Zhang *et al.*, Proc Natl Acad Sci USA **108**, 16900 (2011).
[127] L. Schlapbach, and A. Züttel, Nature **414**, 353 (2001).
[128] G. Sandrock, Journal of Alloys and Compounds **293**, 877 (1999).
[129] F. Schüth, B. Bogdanovi, and M. Felderhoff, Chem. Commun., 2249 (2004).

[130] S.-i. Orimo, Y. Nakamori, J. R. Eliseo, A. Zuttel, and C. M. Jensen, Chemical Reviews **107**, 4111 (2007).
[131] A. C. Dillon, K. M. Jones, T. A. Bekkedahl, C. H. Kiang, D. S. Bethune, and M. J. Heben, Nature **386**, 377 (1997).
[132] C. Liu, Y. Y. Fan, M. Liu, H. T. Cong, H. M. Cheng, and M. S. Dresselhaus, Science **286**, 1127 (1999).
[133] J. L. C. Rowsell, and O. M. Yaghi, J. Am. Chem. Soc. **128**, 1304 (2006).
[134] M. Dinca, and J. R. Long, Angew. Chem. Int. Ed. **47**, 6766 (2008).
[135] G. J. Kubas, J. Acc. Chem. Res. **21**, 120 (1988).
[136] J. Niu, B. K. Rao, and P. Jena, Phys. Rev. Lett. **68**, 2277 (1992).
[137] B. Kiran, A. K. Kandalam, and P. Jena, J. Chem. Phys. **124**, 224703 (2006).
[138] E. Durgun, Y.-R. Jang, and S. Ciraci, Phys Rev. B **76**, 073413 (2007).
[139] Y. Zhao, Y.-H. Kim, A. C. Dillon, M. J. Heben, and S. B. Zhang, Phys. Rev. Letts. **94**, 155504 (2005).
[140] A. B. Phillips, and B. S. Shivaram, Phys. Rev. Letts. **100**, 105505 (2008).
[141] T. Yildirim, and S. Ciraci, Phys. Rev. Letts. **94**, 175501 (2005).
[142] T. Yildirim, J. Íñiguez, and S. Ciraci, Phys. Rev. B **72**, 153403 (2005).
[143] W. Zhou, T. Yildirim, E. Durgun, and S. Ciraci, Phys. Rev. B **76**, 085434 (2007).
[144] Q. Sun, P. Jena, Q. Wang, and M. Marquez, J. Am. Chem. Soc. **128**, 9741 (2006).
[145] M. Yoon, S. Yang, C. Hicke, E. Wang, D. Geohegan, and Z. Y. Zhang, Phys. Rev. Lett. **100**, 206806 (2008).
[146] http://www1.eere.energy.gov/hydrogenandfuelcells/storage/pdfs/targets_onboard_hydro_storage_explanation.pdf.
[147] Q. Sun, Q. Wang, P. Jena, and Y. Kawazoe, J. Am. Chem. Soc. **127**, 14582 (2005).
[148] P. O. Krasnov, F. Ding, A. K. Singh, and B. I. Yakobson, J. Phys. Chem. C **111**, 17977 (2007).
[149] F. A. Cotton, G. Wilkinson, C. A. Murillo, and M. Bochmann, *Advanced Inorganic Chemistry* (Wiley-Interscience, New York, 1999).
[150] M. F. Hawthorne, J. I. Zink, J. M. Skelton, M. J. Bayer, C. Liu, E. Livshits, R. Baer *et al.*, Science **303**, 1849 (2004).
[151] O. K. Farha, A. M. Spokoyny, K. L. Mulfort, M. F. Hawthorne, C. A. Mirkin, and J. T. Hupp, Journal of the American Chemical Society **129**, 12680 (2007).
[152] A. M. S. Omar K. Farha, Karen L. Mulfort, Simona Galli, Joseph T. Hupp, Chad A. Mirkin,, Small **5**, 1727 (2009).
[153] A. K. Singh, A. Sadrzadeh, and B. I. Yakobson, J. Am. Chem. Soc. **132**, 14126 (2010).
[154] G. Kresse, and J. Furthmüller, Phys. Rev. B **54**, 11169 (1996).
[155] G. Kresse, and J. Hafner, Phys. Rev. B **47**, 558 (1993).
[156] P. E. Blöchl, Phys. Rev. B **50**, 17953 (1994).
[157] G. Kresse, and D. Joubert, Phys. Rev. B **59**, 1758 (1999).
[158] J. P. Perdew, K. Burke, and M. Ernzerhof, Phys. Rev. Lett. **77**, 3865 (1996).
[159] D. J. Srolovitz, S. A. Safran, M. Homyonfer, and R. Tenne, Phys. Rev. Lett. **74**, 1779 (1995).
[160] P. G. Collins, and P. Avouris, Scientific American, 62 (2000).

[161] P. Qi, O. Vermesh, M. Grecu, A. Javey, Q. Wang, and H. Dai, Nano Letters **3**, 347 (2003).
[162] J. Kong, N. R. Franklin, C. Zhou, M. G. Chapline, S. Peng, K. Cho, and H. Dai, Science **287**, 622 (2000).
[163] J. Suehiro, G. Zhou, H. Imakiire, W. Ding, and M. Hara, Sensors and Actuators B **105**, 398 (2005).
[164] X. Liu, Z. Luo, S. Han, T. Tang, D. Zhang, and C. Zhou, Appl. Phys. Lett. **86**, 243501 (2005).
[165] H. Chang, J. D. Lee, S. M. Lee, and Y. H. Lee, Appl. Phys. Lett. **79**, 3863 (2001).
[166] J. Zhao, A. Buldum, J. Han, and J. P. Lu, Nanotechnology **13**, 195 (2002).
[167] K. Seo, K. A. Park, C. Kim, S. Han, B. Kim, and Y. H. Lee, J. Am. Chem. Soc. **127**, 15724 (2005).
[168] S. Peng, and K. Cho, Nanotechnology **11**, 57 (2000).
[169] S. Peng, K. Cho, P. Qi, and H. Dai, Chem. Phys. Lett. **387**, 271 (2004).
[170] A. Sadrzadeh, A. A. Farajian, and B. I. Yakobson, Appl. Phys. Lett. **92**, 022103 (2008).
[171] A. A. Farajian, R. V. Belosludov, H. Mizuseki, and Y. Kawazoe, Thin Solid Films **499**, 269 (2006).
[172] A. D. Becke, J. Chem. Phys. **104**, 1040 (1996).
[173] A. A. Farajian, A. Sadrzadeh, O. V. Pupysheva, and B. I. Yakobson, Unpublished.
[174] G. A. Somorjai, *Introduction to Surface Chemistry and Catalysis* (John Wiley & Sons, Inc, New York, 1994).
[175] G. Sun, J. Kurti, M. Kertesz, and R. H. Baughman, J. Phys. Chem. B **107**, 6924 (2003).
[176] J. Zhang, A. Boyd, A. Tselev, M. Paranjape, and P. Barbara, Appl. Phys. Lett. **88**, 123112 (2006).
[177] K. S. Novoselov, A. K. Geim, S. V. Morozov, D. Jiang, Y. Zhang, S. V. Dubonos, I. V. Grigorieva *et al.*, Science **306**, 666 (2004).
[178] S. Dutta, and S. K. Pati, J. Mat. Chem. **20**, 8207 (2010).
[179] K. S. Novoselov, D. Jiang, F. Schedin, T. J. Booth, W. Khotkevich, S. V. Morozov, and A. K. Geim, Proc. Natl. Acad. Sci **102**, 10451 (2005).
[180] K. S. Novoselov, A. K. Geim, S. V. Morozov, D. Jiang, M. I. Katsnelson, I. V. Grigorieva, S. V. Dubonos *et al.*, Nature **438**, 197 (2005).
[181] Y.-W. Son, M. L. Cohen, and S. G. Louie, Phys. Rev. Lett. **97**, 216803 (2006).
[182] K. Nakada, M. Fujita, G. Dresselhaus, and M. S. Dresselhaus, Phys. Rev. B **54**, 17954 (1996).
[183] S. Okada, and A. Oshiyama, Phys. Rev. Lett. **87**, 146803 (2001).
[184] D. A. Abanin, P. A. Lee, and L. S. Levitov, Phys. Rev. Lett. **96**, 176803 (2006).
[185] L. Tapaszto, G. Dobrik, P. Lambin, and L. P. Biro, Nature Nanotech. **3**, 397 (2008).
[186] S. S. Datta, D. R. Strachan, S. M. Khamis, and A. T. C. Johnson, Nano Lett. **8**, 1912 (2008).
[187] D. V. Kosynkin, A. L. Higginbotham, A. Sinitskii, J. R. Lomeda, A. Dimiev, B. K. Price, and J. M. Tour, Nature **458**, 872 (2009).
[188] A. Sadrzadeh, M. Hua, and B. I. Yakobson, Appl. Phys. Lett. **99** (2011).

[189] A. Dobrinsky, A. Sadrzadeh, J. Xu, and B. I. Yakobson, International Journal of High Speed Electronics and Systems **20**, 153 (2011).
[190] D. Porezag, T. Frauenheim, T. Köller, G. Seifert, and R. Kashner, Phys. Rev. B **51**, 12947 (1995).
[191] C. T. White, D. H. Robertson, and J. W. Mintmire, Phys. Rev. B **47**, R5485 (1993).
[192] P. Koskinen, and O. O. Kit, Phys. Rev. Lett. **105**, 106401 (2010).
[193] D. Gunlycke, J. Li, J. W. Mintmire, and C. T. White, Nano Lett. **10**, 3638 (2010).
[194] K. V. Bets, and B. I. Yakobson, Nano Res. **2**, 161 (2009).
[195] R. Rurali, and E. Hernandez, Comput. Mater. Sci. **28**, 85 (2003).
[196] D.-B. Zhang, M. Hua, and T. Dumitrica, J. Chem. Phys. **128**, 084104 (2008).
[197] T. Dumitrica, and R. D. James, J. Mech. Phys. Solids **55**, 2206 (2007).
[198] S. Datta, *Electron Transport in Mesoscopic Systems* (Cambridge University Press, Cambridge, 1995).